LBL-8532

FINAL REPORT
BASALT ALTERATION AND BASALT-WASTE INTERACTION IN THE PASCO BASIN OF WASHINGTON STATE

L. V. Benson, C. L. Carnahan, J. A. Apps, C. A. Mouton, D. J. Corrigan, C. J. Frisch, and L. K. Shomura

Earth Sciences Division
Lawrence Berkeley Laboratory
University of California
Berkeley, California 94720

September 30, 1978

Prepared for Rockwell Hanford Operations
A Prime Contractor to U. S. Department of Energy
under Contract Number W8A-SB8-51760

Work Performed for the U. S. Department of Energy
under Contract W-7405-ENG-48

TABLE OF CONTENTS

LISTS OF TABLES

LIST OF FIGURES

ACKNOWLEDGMENTS

The assistance of Mr. Donn Davy, the Computer Science Group, Lawrence Berkeley Laboratory; Professor H. R. Wenk, the Department of Geology and Geophysics at the University of California, Berkeley; and Mr. Richard Lindbergh, the Materials Research Division, Lawrence Berkeley Laboratory, is gratefully acknowledged.

BASALT ALTERATION AND BASALT-WASTE INTERACTION

L. V. Benson, C. L. Carnahan, J. A. Apps, C. A. Mouton,
D. J. Corrigan, C. J. Frisch, and L. K. Shomura

A. INTRODUCTION L. V. Benson

1. Objectives

The specific objectives of this study are to (1) determine the nature of the minerals which coat vesicle and fracture surfaces in the Grande Ronde Basalt Formation, (2) simulate the mass transfer which led to their precipitation, and (3) predict the mass transfer associated with the dissolution of spent unreprocessed fuel (SURF).

Considerable progress has been made in meeting these objectives. Scanning electron microscopy (SEM), petrographic, x-ray diffraction (XRD), and electron microprobe (EMP) analyses have been made on a series of samples taken from 1100 ft (335.3 m) of core from core hole DC2. Preliminary simulations of the mass transfer associated with basalt dissolution in a thermodynamically closed system have been accomplished. In addition two mass transfer codes have been modified to facilitate data base changes. Thermochemical data for uranium and plutonium have been collected and converted to standard state conditions. These data will be critically evaluated and input to the mass transfer data base in the near future.

2. Rationale

The underlying reasons for acomplishing the objectives itemized above lie in the nature of groundwater-basalt interactions and their effect on radionuclide transport. A prediction of the nature (type, amount, spatial distribution, and rate) of future secondary mineral formation (including precipitation of actinide compounds) in the Pasco Basin can be accomplished only after successful simulation of present-day mass transfer processes.

Characterization of the nature of secondary mineral phases coating fracture and vesicle surfaces in the present day geochemical system serves two purposes: it provides necessary data for mass transfer simulations and it provides data which can be input to future models which take sorption processes into account. In particular secondary mineral phase characterization yields information on the form of the sorptive substrate with which the radionuclides will interact.

3. Previous Work

Past studies of the alteration of continental basalts (Walker, 1951; Walker, 1959; Walker, 1960a; Walker, 1960b; and Roy, 1971) indicate that:

(1) Zeolites, clays, silica and calcite commonly coat the surface of fractures and vesicles (Table 1).

(2) The compositions of the most soluble phases in the host rock influence the compositions and types of secondary minerals.

(3) Secondary minerals exhibit horizontal or, more typically, vertical zonation.

Zonation of secondary minerals involves the redistribution of mass to a thermodynamically more stable state. Reactions that lead to zonation may be caused by changes in the pressure-temperature environment or by introduction of an aqueous solution with which the mineral assemblage is not in equilibrium. In addition, the resulting distribution of mass (secondary minerals) is controlled by the composition of the aqueous solution and the reactant mineral assemblage. To date most workers have attributed the formation of zeolites to reactions driven by changes in pressure or temperature and have ignored reactions driven by compositional disequilibrium. This has led to the suggestion that zeolites are not actively forming today.

Ames (1976) has recently described the secondary mineralogy of five drill cores taken from the Pasco Basin. The distribution of secondary minerals in the two longest cores is summarized in Figure 1. A similar zonation of minerals occurs in both cores; i.e. smectite occurs in the upper portions; and silica (quartz, opal) occurs with clinoptilolite in the lower portions.

4. Geologic Setting

The Columbia River Basalts represent one of the largest accumulations of basalt in the world. The basalt which was extruded in the Miocene covers an area of 2×10^6 km^2. The Pasco Basin located in the northern portion of the Columbia River Plateau is a long-standing structural and topographic low. The basalts of the Pasco Basin, which have a thickness in excess of 1500 m are overlain by lacustrine and fluvial deposits.

The samples described in this study were taken from the Grande Ronde Basalt Formation. The Umtanum Unit located in the lower portion of the Grande Ronde is of particular interest since it has been proposed as a radioactive waste disposal site.

B. RESULTS

1. Petrographic studies C. J. Frisch and L. V. Benson

Twenty-four samples of core from DC2 were selected for detailed thin section petrographic studies. The objectives of these studies were to determine the textural relationships between primary and secondary phases, to determine the sequence of formation of secondary phases coating fractures and vesicles, and to provide a framework for further compositional studies of the mineral phases. The occurrences and relationships of secondary minerals illustrated in Figures 2 and 3 are discussed below.

A positive correlation exists between the amount of original porosity, i.e., the number, size and density of fractures and vesicles, and the extent of alteration of the primary phases. Fractures vary in width from 100 m to 1.5 cm. Occurrences of clay are commonly restricted to the fractures themselves, i.e., plagioclase and clinopyroxene adjacent to fractures remain unaltered. However, in DC2 2314 an alteration halo extends 8 mm on each side of a 1 mm wide fracture. In many of the vesicular samples, the fine-grained basalt matrix has been altered uniformly to a brown clay. Near vesicle walls the alteration is more pronounced. Although relict plagioclase and clinopyroxene remain, the original magmatic texture has been destroyed by alteration to clay (Fig. 2, upper left). In highly vesicular or brecciated samples, the plagioclase laths are mantled with a red-brown clay and clinopyroxene has been altered to clay or fine-grained opaques. In certain instances primary minerals have been completely replaced by a mixture of secondary minerals consisting of zeolite, silica and clay.

Secondary minerals are also common to fractures and vesicles. The general sequence of precipitation was observed to be clay (reddish brown), zeolite and/or silica followed, in some instances, by clay (brown). Secondary minerals common to fractures and vesicles are described in more detail below.

Fractures are often lined with a dark brown clay and in most cases contain either clinoptilolite/heulandite, hereafter referred to as clinoptilolite, or an isotropic phase (tentatively identified as a zeolite) or silica. Clinoptilolite, which can be distinguished by its multilaminar twinning and low birefringence, also occurs along the center of fractures (Fig. 3, upper right). The isotropic zeolite also occurs along the center of fractures but is fine-grained, anhedral and does not exhibit twinning. Silica occurs in the

form of opal, fine-grained aggregates, or thin fibers. In certain instances, thin layers of clinoptilolite and/or opal alternate with up to five layers of clay, each layer exhibiting a distinct color and texture.

Vesicles contain a varied and complex assemblage of secondary minerals (Figs. 2 and 3). The sequence of phases shown in Figure 2 (center) is typical. A dark red-brown clay lines the vesicle walls. Tabular crystals of clinoptilolite formed on the clay surface are intergrown with and are overlain by silica spherulites. In certain cases, a porous mat of clay has formed on the surface of the spherulites.

Representative textures of secondary vesicular minerals are also shown in Figures 2 and 3. Clinoptilolite often occurs as tabular crystals (Fig. 2, bottom left and right), but may also occur in a more prismatic habit (Fig. 3, upper left). In a few cases tabular clinoptilolite can be found intergrown with the spherulitic zeolite (Fig. 2, bottom right).

Several layers of clay are often found lining vesicles. The clays shown in Figure 3 (upper right) include a fine-grained brown variety (Cl-1), similar to the clay which has replaced the basalt matrix, a fibrous green variety (Cl-2), and a fine-grained aggregrate of yellowish-brown clay (Cl-3). In certain samples, vesicles are partially or completely filled with a red-gold clay that exhibits desiccation features (Fig. 3, middle). Clays with a tubular morphology (halloysite?) have also been noted in a few samples.

Silica commonly occurs in the form of spherulites which in Figure 3 (lower left and right) are intergrown with fine-grained opal.

2. Electron microprobe studies - C. J. Frisch and L. V. Benson

The purposes of the electron microprobe studies are to determine the relationship of secondary mineral compositions to primary mineral compositions, and to examine the compositional heterogeneity of secondary minerals as a function of depth in the core, location within single vesicles, location along single crystals, and crystal habit. Initial work has focused on the composition of zeolites and clays.

Polished thin sections were analyzed with an ARL-SEMQ electron microprobe. The following elements were monitored: potassium, sodium, calcium, magnesium, barium, iron, aluminum, silicon, and titanium. Analyses were conducted at an electron beam voltage of 15 kV and a specimen current of 0.012 A. A defocused beam (30 m) was used to minimize volatilization of the alkalies. Preliminary results are discussed below.

Zeolites were divided into three groups on the basis of occurrence and crystal habit, i.e., zeolites found in fractures, zeolites found in vesicles, spherulitic zeolites, and tabular or prismatic zeolites (clinoptilolite). The results of analyses (in oxide weight percent) on selected samples are shown in Table 2. The results are based on anhydrous compositions; water is assumed to make up the remaining 10 to 20 weight percent.

The zeolite groups have distinct compositions as is evident from Table 2. Compositional variation across two morphologically distinct "generations" of zeolite (points 1-10) and along a single clinoptilolite crystal (points 11-13) are illustrated in Figure 5 (DC2 2366). The points in Figure 5 correspond to the sample analyses listed in Table 2. The chemical compositions of the zeolites in Figure 5 are plotted as a function of distance from basalt-secondary mineral boundary shown in Figure 6; the sample numbers are also shown as a reference. Note in Figure 6 (DC2 2366) that both structural (silicon, aluminum) and exchangeable (sodium, potassium) cations exhibit compositional variation. Similar compositional patterns were found for other zeolites in vesicles from DC 2366. However, the compositional patterns of zeolites do not change systematically with depth (Table 2).

Analyses of selected clays are listed in Table 3. The oxide weight percent totals are low, possibly due to high porosity or to the fine-grained texture. The number of ions in the clay formulas, calculated on the basis of 11 oxygen atoms per formula unit, are also shown in Table 3 (the respective sample order is maintained). Assignment of the elements to structural sites was done in the following manner:

(1) All the silicon was assigned to tetrahedral sites, and the remaining vacancies were filled with aluminum.

(2) The remaining aluminum was assigned to octahedral sites. Iron was also assigned to octahedral sites and if any sites remained unfilled, magnesium was added.

(3) The remaining magnesium and calcium, sodium, potassium, and barium were assigned to the exchange site.

The clays also exhibit compositional variation. Figure 5 (DC2 3264) shows three generations of clay, each of which were analyzed six times. The number of ions per formula unit (marked C1-1, C1-2, and C1-3 in Table 3) are plotted in Figure 7. Iron, magnesium, sodium, and calcium ions decrease toward the void, while aluminum and silicon ions increase.

3. X-ray diffraction studies - D. J. Corrigan, L. K. Shomura and L. V. Benson

Sixty-seven samples from 24 depths in DC2 were analyzed with a Norelco diffractometer equipped with a Ni-filtered CuKα radiation source and a graphite monochromator. All samples were ground to less than 50 μm powders and mixed with a silicon standard. The powders were mixed with either water or balsam dissolved in xylene, and the resulting slurry was applied to a glass slide. Sixty-five patterns of zeolite, clay and silica standards were used to interpret the diffraction data. Representative patterns obtained on DC2 samples are shown in Figure 8. A crude attempt to quantify the data was made by multiplying the heights of selected peaks by their widths taken at half the peak height. The results are given in Table 4.

Fractures and breccias are dominated by smectite and silica (quartz, cristobalite, or tridymite). Vesicles are dominated by clinoptilolite, cristobalite and smectite. Vesicles also contain mordenite, erionite, analcime, wairakite, vermiculite, and illite. Plagioclase and pyroxene represent contamination of the sample with primary minerals derived from vesicle and fracture surfaces. The peaks for cristobalite and tridymite are rather broad, suggesting that these phases are disordered. The kind and relative amounts of minerals differ radically among vesicles from the same depth, e.g., DC2 2803X1-6 (Table 4).

4. Scanning electron microscopy - C. A. Mouton and L. V. Benson

Sixty samples of secondary mineral assemblages from 24 depths were examined with an AMR 1000 SEM equipped with an energy dispersive x-ray analyzer (EDAX). The results of this study are shown in Table 5.

Fractures and breccia were found to contain an iron- and magnesium-rich clay or clay and silica with an occasional occurrence of pyrite. Vesicles were found commonly to contain iron- and magnesium-rich clay, silica, and clinoptilolite. In addition, occasional occurrences of aluminosilicate minerals lacking iron and magnesium but containing potassium, sodium and/or calcium were noted. The crystal forms of the minerals together with their compositions suggest that some are feldspars; others may be zeolites or iron- and magnesium-poor clays. In a few instances a fibrous zeolite, possibly erionite or mordenite, was noted. Figures 9 through 12 illustrate the range of crystal form of clinoptilolite, silica, and clay observed in this study. Figures 13 and 14 are EDAX spectra for clinoptilolite, pyrite, and a series of clays with varying compositions.

In 40 of the 45 vesicles studied, clay was the first mineral to have formed; it was iron-rich in 31 cases. It should be noted that clay may have formed first in all cases, but sample preparation may have been insufficient to insure its exposure - i.e., it was covered by later-formed phases. Clinoptilolite and silica alternated as the second and third formed phases and in certain cases they co-precipitated. In 24 instances, an iron-rich clay or a potassium/sodium/calcium-rich aluminosilicate was the final mineral to form. These phases sometimes were found intergrown with a fibrous zeolite or silica. The forms and order of crystallization of secondary mineral assemblages in vesicles from four depths in DC2 are illustrated in Figures 15-19.

5. Preliminary Simulations of Mass Transfer - C. L. Carnahan, L. V. Benson and J. A. Apps

(a) Method

Mass transfer in the basalt-groundwater system underlying the Pasco Basin is controlled largely by chemical reactions between groundwaters and mineral constituents of the basalt. The groundwaters are derived from meteoric waters that have migrated from the earth's surface through aquifers and have been modified chemically by reactions with rocks encountered during transit. They eventually discharge at the earth's surface carrying dissolved constituents resulting from these chemical reactions. Little is known regarding the chemical evolution of the system, including the sequence of chemical reactions that occur and the principal controls affecting chemical composition. Partial to complete equilibrium of the groundwater with the host rock minerals and with secondary alteration products may be achieved; however, little quantitative information is available concerning absolute rates of rock-water chemical reactions.

During the last ten years, a technique has been developed which allows computer simulation of complex chemical reactions between groundwater and rocks. This technique, originally developed by H. C. Helgeson and his co-workers at Northwestern University and described in several papers (Helgeson, 1968; Helgeson, et. al., 1970), has subsequently been modified and refined by others such as the staff of the Kennecott Computer Center in Salt Lake City (FASTPATH code), C. Herrick of the Los Alamos Scientific Laboratory, T. Wolery of Northwestern University (Wolery, 1978), and T. Brown of the University of British Columbia.

The technique permits the calculation of the progressive mass transfer between solids and an aqueous phase as a function of reaction progress, the latter concept having been conceived by De Donder and Van Rysselberghe (1936) to describe changes in the mass of a species undergoing chemical reaction. For computational purposes, one unit of ξ represents addition of one mole of a reactant (rock, mineral, or gas) to a reacting system consisting of an aqueous phase and any initial product phases, the latter consisting of solid mineral phases or gases in equilibrium with the aqueous phase. In practice, an increment of reactant mass is added irreversibly to the reacting system. Chemical elements contained in the added reactant are distributed among possible chemical species. Any product phase found to be supersaturated in the aqueous phase is precipitated until supersaturation is eliminated and chemical equilibrium is achieved between the aqueous and product phases. In closed system simulations, product phases thus formed are allowed to remain within the reacting system and are allowed to react reversibly with the aqueous phase during subsequent reaction progress. Thus, it is not uncommon for a product phase, precipitated at an early stage of reaction progress, to be consumed reversibly and disappear at a later stage. Alternatively, in open system simulations, product phases, once precipitated, are removed from the reacting system and are not allowed to react reversibly with the aqueous phase.

In the simulations to be described, the FASTPATH code was used to study mass transfer in the water-basalt system, with and without the presence of carbon dioxide. Precipitated phases remained in equilibrium with the aqueous phase. Simulations were made at 25, 60, 100, 150, 200, 250, and 300°C.

An idealized chemical composition of the Pomona basalt was used in the simulations. The analysis, upon which the idealized composition is based, was selected from Table III of ARH-ST-137, Vol I (1976), and is given in Table 6 together with the idealized version used for the simulations. It was assumed for this simulation that the basalt consisted primarily of glass.

Each mole of Pomona basalt was allowed to dissolve in water according to the following equation:

$$0.55\ SiO_2 + 0.09\ Al_2O_3 + 0.10\ FeO + 0.12\ MgO + 0.11\ CaO +$$
$$0.025\ Na_2O + 0.005\ K_2O + 1.26H^+ + 0.47\ H_2O =$$

$0.55\ H_4SiO_4 + 0.18\ Al^{+++} + 0.10\ Fe^{++} + 0.12\ Mg^{++} +$
$0.11\ Ca^{++} + 0.05\ Na^{+} + 0.01\ K^{+}$.

An arbitrary aqueous solution containing nominal concentrations of the participating elements was used as the starting solution. The composition is given in Table 7. The pH of the starting solution was assumed to be 7.0. For the simulations in which Pomona basalt reacted with water in the absence of carbon dioxide, each unit of reaction progress (ξ) corresponds to the addition of one mole of Pomona basalt.

A set of simulations with carbon dioxide present as a reactant was done in order to define the effect of pH-buffering by this reactant. Most groundwaters from basaltic terrains contain significant concentrations of inorganic carbon, usually present as the bicarbonate species. The presence of the bicarbonate ion is important because it tends to buffer the pH of the groundwater at a value between 7 and 8, resulting in a different alteration sequence from that observed in carbonate-free systems. The origin of the bicarbonate is not known at present, but may derive from several sources, such as residual magmatic gases, the atmosphere, carbonates precipitated as secondary minerals, and carbon dioxide produced in ancient and existing soil zones. In this set of simulations, the initial groundwater composition was similar to that given in Table 7 except that 10^{-6} mole per kilogram of total carbon was included. The ratio (relative reaction rates) of Pomona basalt to carbon dioxide was set at 9:1, so that each unit of reaction progress corresponds to the addition of 0.9 mole of Pomona basalt and 0.1 mole of carbon dioxide. Although the actual inorganic carbon content of basalts is much less than this ratio, the relative reactivity of carbon dioxide may be much greater, compared with basalt.

For each simulation, the reaction was allowed to progress until the chemical alteration process had stabilized, in the sense that new product phases would not have appeared even if the simulation has been continued indefinitely.

In order to gain insight into the extent of mass transfer occurring in basalt-groundwater systems in the Pasco Basin, comparisons were made between results of the reaction simulation in the presence of carbon dioxide and chemical analyses of real groundwater samples. Four analyses of water from below the Umtanum, from above the Umtanum, from just below the Vantage, and from the Vantage were used as input to the distribution-of-species mode of both the FASTPATH code and a newer code devised by T. Wolery (1978); the

Wolery code is currently being evaluated and tested at LBL. In addition, the Wolery code was used to determine the optimum assemblage of mineral phases which led to removal of all supersaturations from each groundwater sample. Chemical analyses of the four groundwaters are tabulated in Table 8.

(b) Data

A lengthy compilation of results for the simulations with and without the presence of carbon dioxide at 25, 60, 100, 150, 200, 250, and 300°C has been reported elsewhere (Apps, 1978), and will not be repeated here. Instead, the present discussion will be focussed on the simulations at made 60°C, which most closely correspond to mass transfer processes in the basalt-groundwater system.

Table 9 indicates the appearance and disappearance of product mineral phases as the reaction progress variable, ξ, increases. (Chemical formulas of minerals of interest are listed in Table 10.) The variations of quantities of product mineral phases are shown graphically in Figures 20 and 21 for the reaction excluding carbon dioxide. Variations of concentrations of chemical species in the aqueous phase are shown in Figures 22 to 30 for the reaction including carbon dioxide. Variations of concentrations of chemical species in the aqueous phase are shown in Figures 22 to 27 (without carbon dioxide) and Figures 31 to 37 (with carbon dioxide).

Several differences between the simulated reactions, with and without the presence of carbon dioxide, are apparent. The system containing carbon dioxide produces not only the carbonate minerals calcite and siderite, but also four non-carbonate minerals which do not appear in the reaction system lacking carbon dioxide; these four minerals are talc (a magnesium silicate) and the clay minerals kaolinite, calcium montmorillonite, and sodium montmorillonite. A magnesium chlorite appears in both systems at low values of ξ, but is consumed reversibly in the system containing carbon dioxide, whereas talc becomes the more stable magnesium-containing phase at higher values of ξ. Also, tremolite (a calcium-magnesium silicate) and prehnite (a calcium aluminosilicate) are precipitated in the carbonate-free reaction system, but do not reach saturation in the system containing carbonate. Four product mineral phases are common to both reaction systems; these phases are fayalite (an iron silicate), laumontite (a calcium aluminosilicate), adularia (a potassium feldspar) and low albite (a sodium plagioclase).

In comparing the two reaction systems, it is evident that differences in the variations of concentrations of non-carbonate aqueous species and of non-carbonate product mineral phases are attributable principally to the pH-buffering effect of the bicarbonate-carbonic acid equilibrium. This effect can be seen by comparing Figures 22 and 31 which show variations of hydrogen ion concentration during reaction progress. In the carbonate-free system (Figure 22), the hydrogen ion concentration gradually decreases from its initial value of about 10^{-7} molal and eventually stabilizes at a value slightly less than 10^{-11} molal. On the other hand, in the system containing carbon dioxide (Figure 31), the hydrogen ion concentration is never below 0.3×10^{-8} molal and stabilizes at about 10^{-8} molal. The effects of pH-buffering are reflected also by differences between the two reaction systems with respect to distributions of chemical elements among possible aqueous species. For example, striking differences can be seen in the speciations of aluminum (Figures 25 and 34) and iron (Figures 27 and 36); in both cases, concentrations of acidic species are higher by several orders of magnitude in the reaction system containing carbon dioxide.

As the reaction progress variable, ξ, increases, the aqueous phase and the product mineral phases of each simulated reaction system move through a succession of equilibrium states, each such state being characterized by a unique assemblage of aqueous species and product minerals. Eventually a value of ξ is reached in each system beyond which the composition of the aqueous phase is invariant, and further addition of reactants (Pomona basalt, or Pomona basalt plus carbon dioxide) simply causes an increase in the total mass of solid product minerals. At still higher values of ξ, the relative quantities of product minerals become fixed at constant ratios.

For the reaction of Pomona basalt with water in the absence of carbon dioxide, the composition of the aqueous phase is invariant at ξ values exceeding 0.471 (log ξ greater than -0.327), corresponding to the appearance of low albite as the last product mineral phase. The final assemblage of product mineral phases is formed according to the following equation for the irreversible reaction of 1.0 mole of Pomona basalt with water:

$$0.55\ SiO_2 + 0.09\ Al_2O_3 + 0.10\ FeO + 0.12\ MgO + 0.11\ CaO +$$
$$0.025\ Na_2O + 0.005\ K_2O + 0.1663\ H_2O \longrightarrow$$
$$0.02950\ \underset{\text{prehnite}}{Ca_2Al_2Si_3O_{10}(OH)_2} + 0.02133\ \underset{\text{laumontite}}{CaAl_2Si_4O_8(OH)_8} +$$

$$0.01483\ Ca_2Mg_5Si_8O_{22}(OH)_2 + 0.05\ Fe_2SiO_4 +$$
tremolite — fayalite
$$0.05\ NaAlSi_3O_8 + 0.01\ KAlSi_3O_8 + 0.00917\ Mg_5Al_2Si_3O_{10}(OH)_8$$
low albite — adularia — Mg chlorite

For the reaction of Pomona basalt with water in the presence of carbon dioxide, the composition of the aqueous phase is invariant at ξ values exceeding 0.997 (log ξ greater than -0.001), again corresponding to the appearance of low albite as the last product mineral phase. In this case the final assemblage of product mineral phases is formed according to the following equation representing the irreversible reaction of 0.9 mole of Pomona basalt plus 0.1 mole of carbon dioxide with water:

$$0.495\ SiO_2 + 0.081\ Al_2O_3 + 0.09\ FeO + 0.108\ MgO + 0.099\ CaO +$$
$$0.0225\ Na_2O + 0.0045\ K_2O + 0.1\ CO_2 + 0.0918\ H_2O \longrightarrow$$
$$0.0984\ CaCO_3 + 0.0534\ Na_{.33}Al_{2.33}Si_{3.67}O_{10}(OH)_2 +$$
calcite — Na-montmorillonite
$$0.0442\ Fe_2SiO_4 + 0.036\ Mg_3Si_4O_{10}(OH)_2 + 0.0272\ NaAlSi_3O_8 +$$
fayalite — talc — low albite
$$0.009\ KAlSi_3O_8 + 0.0016\ FeCO_3 + 0.0006\ CaAl_2Si_4O_8(OH)_8$$
adularia — siderite — laumontite

Results of the distribution-of-species computations by the FASTPATH code for groundwater samples from below the Umtanum, from above the Umtanum, from the Vantage, and from below the Vantage are shown in Tables 11, 12, 13, and 14. All four groundwaters appear to be supersaturated with respect to a large number of mineral phases; these phases are also listed in the four tables.

Comparison of the concentrations of chemical species, computed from the four groundwater analyses, with the concentrations computed along the reaction path in the Pomona basalt - carbon dioxide - water system (shown in Figures 31 to 37, shows closest agreement for ξ values in the range of -2.0 to -1.5, corresponding to a range in ξ from 0.01 to 0.03. The major exceptions are the aluminum species; the concentrations calculated for the groundwater samples are several orders of magnitude higher than indicated by the reaction path graphs. It is suspected either that the aluminum analyses are in error, or that suspended, colloidal aluminum was incorporated in the chemical analyses.

The Wolery code was used to compute species distributions and mineral saturations for the four groundwaters considered above. The resulting concentrations of chemical species are listed in Tables 15 to 18. Comparison of

these results with the results of the FASTPATH code in Tables 11 to 14 shows general agreement with respect to concentrations of major species. Differences between the two sets of results are attributable to differences in chemical species included in the two codes (for example, the FASTPATH code includes fluoride complexes, while the Wolery code does not) and to differences in the thermodynamic data bases for species common to both codes.

Table 19 lists the minerals found by the Wolery code to be supersaturated in the four groundwaters. Comparison of this list with those in Tables 11 to 14, obtained with the FASTPATH code, reveals a number of differences, particularly with respect to clay minerals. These differences arise because, in general, smectite minerals are treated differently in each program. The FASTPATH code uses end-member components with idealized structural formulas for montmorillonite, while the Wolery code uses end-member components with idealized structural formulas for beidellite, saponite, and nontronite. Illites are assigned different idealized structural formulations in each code.

As pointed out above, comparisons between the results of reaction path simulations in the presence of carbon dioxide and distribution-of-species computations with real groundwaters imply an extent of reaction (ξ) in a closed system in the range of 1×10^{-2} to 3×10^{-2}. At the lower end of this range, the simulations indicate the presence of solid phases consisting of fayalite, laumontite, talc, and a magnesium chlorite. At the higher end of the range, calcite appears in addition to these phases. It should be noted that none of the four groundwaters analyzed appear to be saturated with respect to calcite. Also, the simulations provide no mechanism for precipitation of sodium and potassium up to these values of reaction progress; both elements precipitate at higher values of ξ in the forms of adularia (potassium), sodium montmorillonite, and albite (sodium).

The minerals hypothetically produced by the reaction path simulations do not correspond to secondary minerals actually observed as alteration products in basalts from the Pasco Basin. The observed, secondary minerals, described in detail elsewhere in this report, consist of silica and aluminosilicates, the latter being clays and zeolites. In general, the observed clays contain predominantly iron and magnesium in octahedrally coordinated structural positions, and predominantly magnesium with smaller quantities of calcium and sodium in exchangeable positions. The zeolites (heulandite/clinoptilolite) contain primarily sodium and potassium in exchangeable positions.

The observed clay and zeolite phases were not reproduced by the reaction path simulations because the necessary thermochemical data for these minerals do not exist, and thus are not included in the data base of the reaction code. Instead, the code mimics the evolution of the basalt-carbon dioxide-water system by substituting minerals which are included in the data base. Thus, in the range of ξ below the value at which calcite appears, deposition of calcium is simulated by the zeolite laumontite, which plays the role of the observed heulandite/clinoptilolite. Deposition of iron and magnesium is simulated by fayalite, talc, and the magnesium chlorite, which substitute for the observed iron- and magnesium-rich clays. With this in mind, the agreement between concentrations of aqueous species computed by the reaction simulation and those computed from real groundwater analyses within a relatively small range of ξ seems remarkable. However, it is believed that the agreement for sodium and potassium is fortuitous; the observed secondary phases contain both elements, whereas sodium and potassium are not precipitated in the simulated reaction path until a value of ξ in the range of 0.1 to 1.0 has been attained.

It is apparent that acquisition of thermochemical data (specificaly, standard Gibbs free energies and entropies of formation) for the observed mineral phases would allow more realistic modeling of their depositional history and groundwater evolution than is now possible.

The results of the computations (species distributions and mineral supersaturations) were processed further by the Wolery code to simulate a closed-system precipitation of mineral phases. This simulation consists of the determination of an optimum assemblage of mineral phases, in equilibrium with each aqueous phase, such that the amount of material transferred to the solid phases is just sufficient to remove all supersaturations. The resulting assemblages are listed in Table 20. The reductions of total elemental concentrations in the aqueous phases necessary to produce the solid-phase assemblages were less than one percent for potassium, calcium, and magnesium, while concentrations of total silicon were reduced by approximately fifty percent. Significant reductions of concentrations of aluminum and iron were required; these amounted to about four and twelve orders of magnitude, respectively. The magnitudes of the reductions of concentrations of these two elements indicates that the reported concentrations were erroneously high, due possibly to contamination of water samples or to the inclusion of suspended colloidal

material in the analyses. The appearance of smithsonite and tenorite as hypothetical solid phases is attributed to the anomalously high concentrations of zinc and copper reported. The relatively high values of these elements are probably due to sample contamination. It is interesting to note that the presence of clay and silica minerals in the computed hypothetical solid-phase assemblages is in general agreement with direct observations of similar phases within vesicles and fractures of basalt samples from beneath the Hanford Reservation.

C. DISCUSSION L. V. Benson

A pattern to the alteration of the Pasco Basin basalts is becoming apparent. Vertical zonation of secondary minerals occurs with smectite dominating the upper portion of the stratigraphic column, and clinoptilolite and silica dominating the lower portion. A similar zonation occurs within individual vesicles found in the Grande Ronde Formation. One or more layers of smectite line vesicle walls and is followed in sequence by silica and/or clinoptilolite and clay. Different vesicles sometimes record different portions of the alteration pattern and contain phases not generally observed, (erionite, halloysite, mordenite, analcime, and illite). The loss of record is probably due to the vesicle's isolation from moving fluid; i.e., the fluid pathway leading to or exiting from the vesicle becomes blocked, and mass transport must take place by diffusion instead of advection. This may also explain the precipitation of the "anomalous" phases. If the geochemical system switches from an open system to a closed system mode, then the local composition of the bulk rock will determine, to a large degree, the kinds of secondary phases precipitated. If the composition of the host rock is anomalous, then the secondary phases precipitated as a consequence of its dissolution may also be anomalous.

Fractures and breccia-zones usually contain smectite and/or silica. The absence of clinoptilolite from these features suggests that isolation from the moving fluid has prevented the further compositional evolution (mass transfer) of the system.

The compositions of secondary minerals vary across a single crystal, across an individual layer composed of many crystals, and with location in the stratigraphic column. This compositional heterogeneity may in part be due to ion exchange processes, but it may also reflect and record the original compositional evolution of the aqueous system.

D. RECOMMENDATIONS - L. V. Benson and C. L. Carnahan

The following tasks and inveatigations are recommended to provide increased capability for evaluation of SURF-basalt-water interactions:

1. The data base of the geochemical reaction path code should be updated to include thermochemical data for mineral phases observed in basalts of the Pasco Basin.
2. Composition of the "standard" basalt proposed as input to reaction path simulations should be compared with known basalt compositions in the Pasco Basin to ensure that the input composition is representative of area-wide compositions.
3. In reaction path simulations, relative reaction rates of individual oxide components of input basalt should be regarded as adjustable parameters in order to more closely simulate real dissolution processes.
4. Simulations of basalt-water reactions in both open and closed systems should be made under conditions encompassing the extremes of very high and very low oxidation-reduction potential (Eh), to provide base-line data to which results of SURF-basalt-rock reaction simulations may be compared (see item 5).
5. Simulations of SURF-basalt-water reactions should be made in both open and closed systems, and under conditions of both very high and very low oxidation-reduction potentials (Eh) in order to predict effects of Eh-poising in repositories on contaminant concentrations in effluent groundwater as it migrates toward the biosphere.
6. Sampling and chemical analyses of groundwater should be done throughout the stratigraphic section above, within, and below the Umtanum unit, to provide data to verify the computed evolutions of mass transfer and aqueous phase composition along the groundwater flow path.
7. Continued characterization should be done of cores DC2, DC6 and DH5, including a determination of the types, relative amounts, composition, order of crystallization, and location of secondary phases. These data provide necessary inputs to and checks on mass transfer calculations.
8. The Gibbs free energies of formation of common secondary phases should be estimated and input to the reaction path code data base in order to accurately simulate mass transfer processes common to the natural system.

E. REFERENCES

Ames, L. L., Hanford basalt flow mineralogy, in preparation, 1976.

Apps, J. A. The simulation of reactions between basalt and groundwater: Progress report for the Hanford Waste Isolation Project, Task II, High Level Water Basalt-Interactions, 1978.

De Donder, T., and Van Rysselberghe, P., 1936. Thermodynamic theory of affinity: a book of principles. Stanford: Stanford University Press.

Hay, R. L., Zeolites and zeolitic reactions in sedimentary rocks, Geol. Soc. Am., Special Paper 85, 125 pp., 1966.

Helgeson, H. C., Evaluation of irreversible reactions in geochemical processes involving minerals and aqueous solutions--I. Thermodynamic relations, Geochim. et Cosmochim. Acta, v. 32, 853-877, 1968.

Helgeson, H. C., Brown, T. H., Nigrini, A., and Jones, T.A., Calculations of mass transfer in geochemical processes involving aqueous solutions. Geochimn. et Cosmochim. Acta, v. 34, 569, 1970.

Roy, A. K., Distribution zoning of zeolites in the Deccan Trap basalts of Lonavla--Dehu Road--Poona area, Quart. Jour. Geol. Mining and Met. Soc. of India, 43, 59-73.

Walker, G. P. L., The amygdale minerals in the Tertiary lavas of Ireland. I. The distribution of chabazite habits and zeolites in the Garron Plateau area, County Antrim, Min. Mag., v. 29, 773-791, 1951.

Walker, G. P. L., Some observations on the Antrim basalts and associated dolerite instrusions, Geol. Assoc. Proc., v. 70, 179-205, 1959.

Walker, G. P. L., Zeolite zones and dike distribution in relation to the structure of the basalts of eastern Iceland, Jour. Geol., v. 68, 515-528, 1960a.

Walker, G. P. L., The amygdale minerals in Tertiary lavas of Ireland, III. Regional distribution, Min. Mag., v. 32, 503-527, 1960b.

Wolery, T., Correlation of chemical equilibria. Ph.D. Thesis, Part 2. Evanston: Northwestern University, 1978.

Preliminary Feasibility Study on Storage of Radioactive Wastes in Columbia River Basalts, Two Volumes, ARH-ST-137, Atlantic Richfield Hanford Company, Richland, Wa., November 1976.

TABLES

TABLE 1

Eastern Icelandic Amygdale Minerals (Walker, 1960a)

very abundant	common	rare
analcime	epistilbite	erionite
chabazite	laumontite	gismondine
heulandite	levyne	aragonite
mesolite	phillipsite	epidote
mordenite	apophyllite	
scolecite	celadonite	
stilbite	chlorite	
thomsonite	gyrolite	
calcite		
chalcedony		
opal		
quartz		

Secondary Minerals in the Deccan Trap Basalts (Roy, 1971)

apophyllite	calcite
stilbite	quartz
natrolite	chalcedony
heulandite	chlorite
mesolite	epidote
scolecite	
chabazite	
thomsonite	
gyrolite	
analcime	

TABLE 1 (cont.)

Amygdale Minerals in the Tertiary Lavas of Ireland (Walker, 1906b)*

relative abundance	percent of localities
chabazite	84
thomsonite	53
calcite	40
analcime	31
levyne	27
natrolite	23
mesolite	10
stilbite	9
gmelinite	9
heulandite	7
phillipsite	6
aragonite	6
apophyllite	5
quartz	
chalcedony	
opal	
gismondine	<1
scolecite	<1
laumontite	<1
mordenite	<1

*Also present but not studied, cryptocrystalline materials such as celadonite and saponite.

TABLE 2. ZEOLITE COMPOSITIONS OF SELECTED SAMPLES FROM DC-2

Analysis	Number	SiO_2	Al_2O_3	FeO	MgO	CaO	BaO	Na_2O	K_2O	Total
Zeolites in Fractures										
	Depth 2314 ft (705.3 m)									
A	2	68.72	10.82	.47	.01	.61	NA	2.25	2.96	85.84
A	16-20	70.80	10.64	.49	.02	.61	NA	2.16	2.44	87.16
A	21-25	69.05	10.79	.46	.02	.62	NA	2.52	2.84	86.31
Spherulitic Zeolites										
	Depth 2366 ft (721.2 m)									
A	22-24	62.95	16.19	.15	0.0	.17	1.28	4.57	5.17	90.48
A	26-30	62.31	15.94	.05	.01	.13	1.38	4.54	5.19	89.53
A	31-34	62.74	16.13	.22	.01	.13	1.43	4.79	4.94	90.39
A	35	63.72	15.73	.09	.02	.14	1.23	4.98	4.67	90.59
A	41-44	63.28	15.73	.18	.03	.12	1.48	4.65	4.84	90.30
Clinoptilolite										
	Depth 2366 ft (721.2 m)									
C	1-7	65.72	13.04	.12	.05	1.48	.63	2.60	3.39	87.23
C	8	67.14	12.43	.02	0.0	.81	.47	2.91	3.65	87.43
C	9	69.50	12.73	.03	.01	.95	.39	2.80	3.36	89.77
C	10	69.61	12.86	0.0	0.0	.79	.46	2.48	3.48	89.69
C	11	66.87	12.22	0.0	0.0	.83	.40	2.00	3.22	85.53
C	12	67.03	11.93	.01	0.0	.83	.36	1.61	2.66	84.43
C	13	67.11	12.36	.02	0.0	.69	.26	1.53	2.61	84.58
	Depth 2632 ft (802.2 m)									
A	1-20	70.38	12.25	.25	.04	.99	NA	2.52	3.87	90.35
A	21-32	70.11	12.17	.18	.01	.96	NA	2.62	4.07	90.13
	Depth 2666 ft (812.6 m)									
A	1-6	69.84	11.96	.08	0.0	.73	.31	2.61	3.26	88.81
A	7-9	71.43	11.82	.15	.01	.60	.35	2.78	3.69	90.84
A	11-16	67.59	11.67	.02	0.0	.68	.34	2.46	3.07	85.83
A	17-21	66.95	11.72	.03	0.0	.72	.34	2.41	3.13	85.29
	Depth 2883 ft (878.7 m)									
A	15-21	76.19	12.40	.13	.01	.86	.34	3.39	.01	93.34
	Depth 3264 ft (994.9 m)									
D	19-26	73.92	11.74	.11	.01	2.61	.04	2.82	0.0	91.25
E	1-2	69.04	13.73	.05	.01	1.91	.34	4.17	.01	89.24
G	19-23	69.22	12.35	.16	.01	1.70	.34	3.13	.01	86.91
G	25-28	67.21	12.32	.04	.01	1.47	.25	2.48	.01	83.77

NA = Not analyzed

TABLE 3. CHEMICAL COMPOSITIONS OF CLAY IN DC-2

Analysis	Number	SiO_2	TiO_2	Al_2O_3	FeO	MgO	CaO	BaO	Na_2O	K_2O	H_2O*	Total
Clays in Fractures												
Depth 2314 ft (705.3 m)												
A	8-15	43.51	.10	5.63	25.62	5.77	1.55	NA	.73	.79	7.08	90.78
Depth 2507 ft (764.1 m)												
A	7-11	46.14	.31	4.81	22.79	7.53	1.40	NA	1.18	.39	7.33	91.88
Depth 2883 ft (878.7 m)												
A	25-34	53.77	NA	11.83	11.65	.91	5.22	.17	4.47	.01	8.16	95.99
Clays in Vesicles												
Depth 2632 (802.2 m)												
C	1-6	42.12	.23	3.41	25.75	3.33	1.11	NA	1.02	.57	6.52	84.05
Clays Lining Vesicle Walls												
Depth 3264 (994.9 m)												
E	2-6	49.25	NA	6.73	18.12	4.18	1.13	.01	.68	.01	7.29	87.36
E	7-10	43.65	NA	5.70	18.85	4.19	1.52	.01	.80	.01	6.63	81.34
E	12-18	53.74	NA	7.28	18.24	2.74	.73	.03	.44	.02	7.[illegible]	90.88

Ions Calculated on the Basis of 11 Oxygens

	Si^{TET}	Al^{TET}	Al^{OCT}	Fe^{OCT}	Mg^{OCT}	$X_{Fe}{}^{OCT}$	Mg^{EXC}	Ca^{EXC}	Na^{EXC}	K^{EXC}	Ba	Ti
	3.682	.318	.241	1.816	--	.652	.727	.142	.122	.081	--	.005
	3.776	.224	.238	1.559	.203	.572	.717	.123	.187	.039	--	.020
	3.955	.045	.980	.716	.102	.398	--	.411	.636	--	.004	--
	3.875	.125	.240	1.979	--	.739	.459	.111	.177	.066	--	.017
CL-1	4.054	--	.653	1.246	.101	.516	.413	.099	.109	--	--	--
CL-2	3.942	.058	.550	1.423	.027	.561	.538	.147	.141	--	--	--
CL-3	4.197	--	.667	1.192	.141	.547	.178	.061	.066	--	--	--

*Stoichiometric H_2O.

NA = Not analyzed.

TABLE 4
X-ray Diffraction Data *

Sample Number	Quartz	Trid-ymite	Cristo-balite	Clinop-tilolite	Smectite	Other
DC2 2206X1(v)				53	47	
DC2 2206X2(v)			24		6	Pl(70)
DC2 2206X3(v)			16	68	16	
DC2 2206X4(v)			36	64		
DC2 2240X1'(f)					100	
DC2 2240X1"(f)					100	
DC2 2240X2'(f)	2	77			21	
DC2 2240X2"(f)	2	49			49	
DC2 2282X1(f)	3	30	62	5		
DC2 2314X1(f)					100	
DC2 2319X1(v)			6	28	11	Pl(55)
DC2 2319X2(v)				84	16	
DC2 2319X3(v)	2			90		Pl(8)
DC2 2319X4(v)				95	5	
DC2 2319X5(v)				79		W(21)
DC2 2319X6(v)				11	78	Pl(11)
DC2 2347X2(v)	88	1		1		
DC2 2354X2(v)			2	95	3	
DC2 2354X3'(v)				53	47	
DC2 2354X3"(v)			19	67	14	
DC2 2354X4(v)				93	7	
DC2 2354X5(v)	20			55	5	Pl(20)
DC2 2359X1(v)			55	17	11	U(16)
DC2 2359X2(v)			28	49	13	U(10)
DC2 2359X3(v)	27			43		Sa(30)
DC2 2359X4(v)			48	31	21	
DC2 2366X1(v)			23	66		A(6)E(2)U(2)
DC2 2366X2(v)				65		E(35)

*See note following Table 4.

TABLE 4 (cont.)
X-ray Diffraction Data*

Sample Number	Quartz	Trid-ymite	Cristo-balite	Clinop-tilolite	Smectite	Other
DC2 2402X2(f)					100	
DC2 2402X2'(f)	59		37	4		
DC2 2402X3(f)				86	14	
DC2 2448X1(v)		9	89	2		
DC2 2448X2(v)			26	41	5	U(28)
DC2 2507X1(f)	14		63	2	21	
DC2 2561X1(f)		31	59	1	6	Pl(3)
DC2 2632X1(v)			4	82		Pl(7)Pyx(7)
DC2 2632X2(v)				92	8	
DC2 2632X3(v)	5		36	13	2	Pl(44)
DC2 2666X1(v)	18	15	45	22		
DC2 2666X2(v)					100	
DC2 2666X3(f)	92		8			
DC2 2749X1(b)	6				81	U(13)
DC2 2749X3(v)	6			90	1	U(3)

*See note following Table 4.

TABLE 4 (cont.)
*X-ray Diffraction Data**

Sample Number	Quartz	Trid-ymite	Cristo-balite	Clinop-tilolite	Smectite	Other
DC2 2803X1(v)	58		2	21	10	Pyx(5)Pl(4)
DC2 2803X2(v)	49		1	3	47	
DC2 2803X3(v)	3		97	17		
DC2 2803X4'(v)	10		57	1	15	
DC2 2803X4"(v)	56		4	1	39	
DC2 2803X5(v)	21		5	10	61	Pl(3)
DC2 2803X6(v)	96			2	2	
DC2 2868X1(b)				8	90	Pl(2)
DC2 2883X1(f)		33	65	2		
DC2 2883X2(v)		29	69	2		
DC2 2883X3(v)			19	4	4	Pl(73)
DC2 2926X1(f)		50		6	40	Pl(4)
DC2 2955X1(v)		27	71	2		
DC2 2955X2(v)		25	45	16		P(14)
DC2 2960X1(v)			8	77	2	Pl(6)Pyx(7)
DC2 2960X2(v)			19	68		Pl(5)Pyx(8)
DC2 2960X3(v)			34	53		Pl(6)Pyx(7)
DC2 3181X1(v)					87	U(2)C(8) U(2)
DC2 3181X1'(v)			1		53	Pl(2)V(44)
DC2 3264X1(v)				10	10	I(80)
DC2 3264X2(v)	100					
DC2 3264X3(v)				18	24	Mo(23)V(24)U(10)
DC2 3264X3'(v)				10	20	Mo(70)
DC2 3264X3"(v)	12		38	33	7	Mo(10)

*Numbers in column 2, 3, 4, 5, 6, and 7 are percentages contributed by indicated phases to total peak area in x-ray diffraction spectra. Meanings of symbols in column 1 are: b, brecciated; f, fracture; v, vesicle; and in column 7 are: A, analcite; C, calcite; E, erionite; I, illite; Mo, mordenite; P, pyrite; Pl, plagioclase; Pyx, pyroxene; Sa, sanidine; T, tridymite; U, unknown; V, vermiculite; W, wairakite.

TABLE 5. SCANNING ELECTRON MICROSCOPE DATA, CORE DC2

Number*	Depth (m)	Crystallization Sequence**
DC2 2206S1(v)	673.4	Cl→C/H→Si
S2A(v)		Cl→C/H→Cl
S2B(v)		Cl→C/H→Si
S3(v)		C/H→Si-K
S4(v)		Cl→Si→Cl
DC2 2240S1,2(f)	682.8	Cl
DC2 2282S1(f)	695.6	Si→Cl
DC2 2314S1(f)	705.3	Cl
DC2 2319S1(v)	706.8	Cl
S2(v)		Cl
S3(v)		Cl
S4A(v)		Cl
S4B(v)		Cl
S5A(v)		Cl→KCaNa-Cl
S5B(v)		Cl
S5C(v)		KCa→Cl
DC2 2347S1(v)	715.4	Cl→Si
DC2 2354S1(v)	717.5	Cl→Si

TABLE 5 (cont.)

Number*	Depth (m)	Crystallization Sequence**
DC2 2359S1A(v)	719.0	Na→K→Cl
S1B(v)		Cl
S2A(v)		KNa→C/H→Cl
S2B(v)		NaK→Cl→C/H→Cl
DC2 2366S1A(v)	721.2	Cl-Ap-Si→Si→Cl
S1B(v)		Cl→KNa→Si→Cl
DC2 2402S1,2,3(f)	732.1	Cl→Si→Cl→Cl
DC2 2448S1(v)	746.2	Cl
S2(v)		Si→Cl-K→Si→Cl-K
DC2 2507S1(f)	764.1	Si
DC2 2561S1(f)	780.6	Cl→Si-Cl
DC2 2632S1(v)	802.2	Cl→K
S2(b)		Cl
S3A(v)		C/H→Cl
S3B(v)		C/H-Cl→Cl→Si
S3C(v)		Cl
S3D(v)		Cl→C/H→Cl-Si
S3E(v)		Cl→C/H-Si
DC2 2666S2A(v)	812.6	Si
S1B(v)		K→Si→Cl
S1C(v)		Cl→Si
S1D(v)		K→Si→Cl-Ca
S2(f)		Cl-Si-K→Si

Table 5 (cont.)

Number	Depth (m)	Crystallization Sequence**
DC2 2749S1A(v)	837.9	Cl→Si-Cl
S1B(v)		Cl→C/H→Cl-KCa
S1C(b)		Cl
DC2 2803S1(v)	854.4	Cl→K→Si-Cl
S2(v)		K→Cl
S2(v)		NaK→Cl→K→Cl-Si→Cl
DC2 2831S1(v)	862.9	Cl
DC2 2868S1 (b)	874.2	Cl
DC2 2883S1(f)	878.7	Si→Cl
S2(f)		Cl
DC2 2926S1(f)	891.8	P-Cl
DC2 2955S1(f)	900.7	Si-P→Cl→Si
DC2 2960S1A(v)	902.2	Si-C/H→Cl→Cl-Si
S1B(f)		Cl
DC2 3264S1(v)	994.9	KNaCa→Si→C/H→Cl
S2(v)		Cl→Si-Cl→Si
S4(v)		Si→Cl→Si

*b: brecciated; f: fracture; v: vesicle.
**C/H: clinoptilolite/heulandite
Cl: iron-magnesium-rich clay
Ap: apatite
P: pyrite
Si: silica
K, Ca, Na: aluminosilicate minerals lacking iron and magnesium and containing potassium, calcium, and/or sodium.

TABLE 6

Chemical Composition of Pomona Basalt
Used in the Simulation of
The Reaction Between Basalt and Groundwater

	Pomona, Al266 (Wt.%)	Pomona Idealized (Wt.%)	Pomona Idealized (Mole Fraction)
SiO_2	52.6	53.46	0.55
Al_2O_3	14.4	14.63	0.09
FeO	11.0	11.18	0.10
MgO	7.6	7.72	0.12
CaO	9.7	9.86	0.11
Na_2O	2.4	2.44	0.025
K_2O	0.7	0.71	0.005
TiO_2	1.6	0.00	0.00
MnO	0.19	0.00	0.00
SrO	0.016	0.00	0.00
P_2O_5	-.-	0.00	0.00
		100.00	1.00

TABLE 7

Initial Composition of Groundwater
Expressed as Basic Components

	Concentration (moles/kg)
Na^{+}	1×10^{-6}
Mg^{++}	1×10^{-6}
Al^{+++}	3.2×10^{-17}
H_4SiO_4	1×10^{-6}
Cl^{-}	0.714×10^{-5}
Ca^{++}	1×10^{-6}
Fe^{++}	1×10^{-6}
H^{+}	1×10^{-7}

TABLE 8

Chemical Analyses of Groundwater From Basalt Horizons Below the Hanford Reservation, Richland, Washington[1)]

Component[2)]	Below Umtanum (ppm)	Umtanum (ppm)	Vantage (ppm)	Below Vantage (ppm)
HCO_3^-	42.8	67.3	64.3	93.8
CO_3^{-2}	0	0	0	0
Cl^-	16.2	8.75	9.50	9.25
SO_4^{-2}	23	15	82	33
B	<0.05	<0.05	<0.05	0.13
Ca^{+2}	6.5	8.5	30	16
Mg^{+2}	1.0	2.2	4.5	2.7
K^+	9.0	7.7	20.0	18.6
Na^+	30	25	52	55
SiO_2	22.5	22.5	22.5	21.2
F^-	0.72	0.7	0.58	0.45
Al^{+3}	0.37	0.10	0.10	0.10
Zn^{+2}	2.56	39	0.024	0.053
Cu	0.02	0.05	0.01	0.016
Fe^{+2}	0.075	<0.02	0.06	0.093
pH	7.3	7.4	7.5	7.9

1) Analyses performed by the United States Testing Company for ARHCo, received on 5/11/77 (Report No. 1270P).

2) Analyses also included conductivity, NO_3-N, dissolved solids, B, TOC, Hg, Sb, Ba, Cd, Cr, Co, Pb, Mo, Ag, and Mn.

TABLE 9

Changes of Product Phase Assemblages During Simulated Reactions of Pomona Basalt and Water

Log ξ Value, CO_2 Absent[1]	Event	Log ξ Value, CO_2 Present[2]
- 5.78[3]	corundum precipitates	- 5.65[3]
- 4.76	fayalite precipitates	- 4.66
- 4.65	chlor Mg precipitates	- 4 52[3]
- 3.88[3]	kyanite precipitates	- 3.86[3]
- 3.80	corundum consumed	- 3.79
———[4]	kaolinite precipitates	- 3.53[3]
- 3.58	laumontite precipitates	(occurs later)
- 3.27	kyanite consumed	- 3.43
(occurs earlier)	laumontite precipitates	- 3.42
- 2.86	tremolite precipitates	———[4]
———[4]	kaolinite consumed	- 2.95
———[4]	talc precipitates	- 2.74
———[4]	calcite precipitates	- 1.82
———[4]	kaolinite precipitates	- 1.51[3]
———[4]	chlor Mg consumed	- 1.39
———[4]	Ca montmorillonite precipitates	- 1.29[3]
———[4]	kaolinite consumed	- 1.04
———[4]	siderite precipitates	- .95
- 1.50	adularia precip. [illegible]es	- .92
- 1.01	prehnite precip[illegible]ate	———[4]
———[4]	Na montmorillonite precipitates	- .24
———[4]	Ca montmorillonite consumed	- .18
- .33	low albite precipitates	- .00

Notes: 1. One unit of ξ corresponds to addition of 1.0 mole of Pomona basalt per kilogram of water.

TABLE 10

Chemical Formulas of Mineral Phases

Mineral Name	Chemical Formula
adularia	$KAlSi_3O_8$
calcite	$CaCO_3$
Ca-montmorillonite	$Ca_{.165}Al_{2.33}Si_{3.67}O_{10}(OH)_2$
Mg chlorite	$Mg_5Al_2Si_3O_{10}(OH)_8$
corundum	Al_2O_3
fayalite	Fe_2SiO_4
kaolinite	$Al_2Si_2O_5(OH)_4$
kyanite	Al_2SiO_5
laumontite	$CaAl_2Si_4O_8(OH)_8$
low albite	$NaAlSi_3O_8$
Na-montmorillonite	$Na_{.33}Al_{2.33}Si_{3.67}O_{10}(OH)_2$
prehnite	$CaAl_2Si_3O_{10}(OH)_2$
siderite	$FeCO_3$
talc	$Mg_3Si_4O_{10}(OH)_2$
tremolite	$Ca_2Mg_5Si_8O_{22}(OH)_2$

TABLE 11

Concentrations of Aqueous Species and List of Supersaturated Minerals, Water from Below the Umtanum (FASTPATH code)

Species	Concentration (moles/kg)	Species	Concentration (moles/kg)	Supersaturated Minerals
Na^{+}	$.89 \times 10^{-3}$	$ZnCl^{+}$	$.38 \times 10^{-7}$	corundum
Mg^{+2}	$.39 \times 10^{-4}$	$ZnCl_2$	$.24 \times 10^{-10}$	gibbsite
Al^{+3}	$.16 \times 10^{-10}$	$ZnCl_3^{-}$	$.91 \times 10^{-14}$	microcline
H_4SiO_4	$.37 \times 10^{-3}$	$ZnCl_4^{-2}$	$.21 \times 10^{-17}$	low albite
Cl^{-}	$.46 \times 10^{-3}$	$ZnSO_4$	$.14 \times 10^{-5}$	anorthite
K^{+}	$.23 \times 10^{-3}$	$Al(OH)_2^{+}$	$.12 \times 10^{-4}$	kaolinite
Ca^{+2}	$.16 \times 10^{-3}$	$H_3SiO_4^{-}$	$.18 \times 10^{-5}$	Na-montmorillonite
Fe^{+2}	$.12 \times 10^{-5}$	HSO_4^{-}	$.97 \times 10^{-9}$	muscovite
Zn^{+2}	$.38 \times 10^{-4}$	HCO_3^{-}	$.64 \times 10^{-3}$	illite
CO_3^{-2}	$.71 \times 10^{-6}$	H_2CO_3	$.69 \times 10^{-4}$	biotite
SO_4^{-2}	$.23 \times 10^{-3}$	HCl	$.17 \times 10^{-16}$	kyanite
F^{-}	$.37 \times 10^{-4}$	$MgOH^{+}$	$.26 \times 10^{-8}$	adularia
$Al(OH)^{+2}$	$.23 \times 10^{-7}$	$FeOH^{+}$	$.10 \times 10^{-6}$	high sanidine
$Al(OH)_4^{-}$	$.12 \times 10^{-5}$	$CaOH^{+}$	$.46 \times 10^{-9}$	dickite
KSO_4^{-}	$.30 \times 10^{-6}$	$Fe(OH)_2$	$.99 \times 10^{-9}$	halloysite
$NaCO_3^{-}$	$.97 \times 10^{-8}$	AlF_5^{-2}	$.19 \times 10^{-12}$	K-montmorillonite
$NaSO_4^{-}$	$.19 \times 10^{-5}$	AlF_2^{+}	$.57 \times 10^{-7}$	Ca-montmorillonite
$CaCO_3$	$.12 \times 10^{-6}$	AlF^{+2}	$.43 \times 10^{-8}$	Mg-montmorillonite
$CaHCO_3^{+}$	$.15 \times 10^{-5}$	AlF_3	$.21 \times 10^{-7}$	andalusite
$CaSO_4$	$.49 \times 10^{-5}$	AlF_4^{-}	$.20 \times 10^{-9}$	sillimanite
$MgCO_3$	$.47 \times 10^{-7}$	AlF_6^{-3}	$.26 \times 10^{-16}$	25 SW montmorillonite
$MgHCO_3^{+}$	$.16 \times 10^{-6}$	HF	$.27 \times 10^{-8}$	K-alunite
$MgSO_4$	$.15 \times 10^{-5}$	MgF^{+}	$.42 \times 10^{-6}$	chlorite (Mg)
$FeCl^{+}$	$.25 \times 10^{-8}$	H^{+}	$.53 \times 10^{-7}$	laumontite
$FeSO_4$	$.30 \times 10^{-7}$	OH^{-}	$.21 \times 10^{-6}$	prehnite
				wairakite
				zoisite

TABLE 12

Concentrations of Aqueous Species and List of Supersaturated Minerals, Water from above the Umtanum (FASTPATH code).

Species	Concentration (moles/kg)	Species	Concentration (moles/kg)	Supersaturated Minerals
Na^{+}	$.61 \times 10^{-3}$	$ZnCl^{+}$	$.57 \times 10^{-7}$	corundum
Mg^{+2}	$.87 \times 10^{-4}$	$ZnCl_2$	$.19 \times 10^{-10}$	gibbsite
Al^{+3}	$.27 \times 10^{-11}$	$ZnCl_3^{-}$	$.40 \times 10^{-14}$	microcline
H_4SiO_4	$.37 \times 10^{-3}$	$ZnCl_4^{-2}$	$.51 \times 10^{-18}$	low albite
Cl^{-}	$.25 \times 10^{-3}$	$ZnSO_4$	$.25 \times 10^{-5}$	anorthite
K^{+}	$.20 \times 10^{-3}$	$Al(OH)_2^{+}$	$.32 \times 10^{-5}$	kaolinite
Ca^{+2}	$.20 \times 10^{-3}$	$H_3SiO_4^{-}$	$.22 \times 10^{-5}$	Na-montmorillonite
Fe^{+2}	$.32 \times 10^{-6}$	HSO_4^{-}	$.49 \times 10^{-9}$	muscovite
Zn^{+2}	$.11 \times 10^{-3}$	HCO_3^{-}	$.10 \times 10^{-2}$	illite
CO_3^{-2}	$.14 \times 10^{-5}$	H_2CO_3	$.87 \times 10^{-4}$	biotite
SO_4^{-2}	$.15 \times 10^{-3}$	HCl	$.74 \times 10^{-17}$	kyanite
F^{-}	$.36 \times 10^{-4}$	$MgOH^{+}$	$.72 \times 10^{-8}$	adularia
$Al(OH)^{+2}$	$.48 \times 10^{-8}$	$FeOH^{+}$	$.34 \times 10^{-7}$	high sanidine
$Al(OH)_4^{-}$	$.49 \times 10^{-6}$	$CaOH^{+}$	$.76 \times 10^{-9}$	dickite
KSO_4^{-}	$.16 \times 10^{-6}$	$Fe(OH)_2$	$.41 \times 10^{-9}$	halloysite
$NaCO_3^{-}$	$.13 \times 10^{-7}$	AlF_5^{-2}	$.26 \times 10^{-13}$	K-montmorillonite
$NaSO_4^{-}$	$.84 \times 10^{-6}$	AlF_2^{+}	$.86 \times 10^{-8}$	Ca-montmorillonite
$CaCO_3$	$.31 \times 10^{-6}$	AlF^{+2}	$.69 \times 10^{-9}$	Mg-montmorillonite
$CaHCO_3^{+}$	$.31 \times 10^{-5}$	AlF_3	$.32 \times 10^{-8}$	andalusite
$CaSO_4$	$.41 \times 10^{-5}$	AlF_4^{-}	$.28 \times 10^{-10}$	sillimanite
$MgCO_3$	$.21 \times 10^{-6}$	AlF_6^{-3}	$.35 \times 10^{-17}$	25 SW montmorillonite
$MgHCO_3^{+}$	$.59 \times 10^{-6}$	HF	$.21 \times 10^{-8}$	chlorite (Mg)
$MgSO_4$	$.21 \times 10^{-5}$	MgF^{+}	$.59 \times 10^{-6}$	laumontite
$FeCl^{+}$	$.35 \times 10^{-9}$	H^{+}	$.42 \times 10^{-7}$	prehnite
$FeSO_4$	$.51 \times 10^{-8}$	OH^{-}	$.26 \times 10^{-6}$	wairakite
				zoisite

TABLE 13

Concentrations of Aqueous Species and List of Supersaturated Minerals, Water from the Vantage (FASTPATH code)

Species	Concentration (moles/kg)	Species	Concentration (moles/kg)	Supersaturated Minerals
Na^{+}	$.64 \times 10^{-3}$	$Al(OH)_2^{+}$	$.30 \times 10^{-5}$	corundum
Mg^{+2}	$.16 \times 10^{-3}$	$H_3SiO_4^{-}$	$.28 \times 10^{-5}$	gibbsite
Al^{+3}	$.18 \times 10^{-11}$	HSO_4^{-}	$.19 \times 10^{-8}$	microcline
H_4SiO_4	$.37 \times 10^{-3}$	HCO_3^{-}	$.99 \times 10^{-3}$	low albite
Cl^{-}	$.26 \times 10^{-3}$	H_2CO_3	$.65 \times 10^{-4}$	anorthite
K^{+}	$.51 \times 10^{-3}$	HCl	$.62 \times 10^{-17}$	kaolinite
Ca^{+2}	$.68 \times 10^{-3}$	$MgOH^{+}$	$.16 \times 10^{-7}$	talc
Fe^{+2}	$.90 \times 10^{-6}$	$FeOH^{+}$	$.11 \times 10^{-6}$	Na-montmorillonite
CO_3^{-2}	$.19 \times 10^{-5}$	$CaOH^{+}$	$.30 \times 10^{-8}$	muscovite
SO_4^{-2}	$.77 \times 10^{-3}$	$Fe(OH)_2$	$.17 \times 10^{-8}$	illite
F^{-}	$.25 \times 10^{-4}$	AlF_5^{-2}	$.25 \times 10^{-14}$	biotite
$Al(OH)^{+3}$	$.38 \times 10^{-8}$	AlF_2^{+}	$.24 \times 10^{-8}$	kyanite
$Al(OH)_4^{-}$	$.73 \times 10^{-6}$	AlF^{+2}	$.29 \times 10^{-9}$	adularia
KSO_4^{-}	$.20 \times 10^{-5}$	AlF_3	$.59 \times 10^{-9}$	high sanidine
NaCO	$.17 \times 10^{-7}$	AlF_4^{-}	$.37 \times 10^{-11}$	dickite
$NaSO_4^{-}$	$.42 \times 10^{-5}$	AlF_6^{-3}	$.25 \times 10^{-18}$	halloysite
$CaCO_3$	$.11 \times 10^{-5}$	HF	$.11 \times 10^{-8}$	K-montmorillonite
$CaHCO_3^{+}$	$.93 \times 10^{-5}$	MgF^{+}	$.51 \times 10^{-5}$	Ca-montmorillonite
$CaSO_4$	$.61 \times 10^{-4}$	H^{+}	$.34 \times 10^{-7}$	Mg-montmorillonite
$MgCO_3$	$.43 \times 10^{-6}$	OH^{-}	$.34 \times 10^{-6}$	andalusite
$MgHCO_3^{+}$	$.97 \times 10^{-6}$			sillimanite
$MgSO_4$	$.18 \times 10^{-4}$			25 SW montmorillonite
$FeCl^{+}$	$.99 \times 10^{-9}$			K-alunite
$FeSO_4$	$.64 \times 10^{-7}$			chlorite (Mg)
				laumontite
				prehnite
				wairakite
				zoisite

TABLE 14

Concentrations of Aqueous Species and List of Supersaturated Minerals, Water from Just Below the Vantage (FASTPATH code).

Species	Concentration (moles/kg)	Species	Concentration (moles/kg)	Supersaturated Minerals
Na^{+}	$.10 \times 10^{-2}$	$Al(OH)_2^{+}$	$.15 \times 10^{-5}$	corundum
Mg^{+2}	$.10 \times 10^{-3}$	$H_3SiO_4^{-}$	$.66 \times 10^{-5}$	gibbsite
Al^{+3}	$.13 \times 10^{-12}$	HSO_4^{-}	$.33 \times 10^{-9}$	microcline
H_4SiO_4	$.35 \times 10^{-3}$	HCO_3^{-}	$.15 \times 10^{-2}$	low albite
Cl^{-}	$.26 \times 10^{-3}$	H_2CO_3	$.40 \times 10^{-4}$	anorthite
K^{+}	$.47 \times 10^{-3}$	HCl	$.24 \times 10^{-17}$	kaolinite
Ca^{+2}	$.36 \times 10^{-3}$	$MgOH^{+}$	$.26 \times 10^{-7}$	talc
Fe^{+2}	$.12 \times 10^{-5}$	$FeOH^{+}$	$.40 \times 10^{-6}$	Na-montmorillonite
CO_3^{-2}	$.69 \times 10^{-5}$	$CaOH^{+}$	$.41 \times 10^{-8}$	muscovite
SO_4^{-2}	$.32 \times 10^{-3}$	$Fe(OH)_2$	$.15 \times 10^{-7}$	illite
F^{-}	$.22 \times 10^{-4}$	AlF_5^{-2}	$.10 \times 10^{-15}$	biotite
$Al(OH)^{+2}$	$.71 \times 10^{-9}$	AlF_2^{+}	$.15 \times 10^{-9}$	kyanite
$Al(OH)_4^{-}$	$.23 \times 10^{-5}$	AlF^{+2}	$.20 \times 10^{-10}$	adularia
KSO_4^{-}	$.82 \times 10^{-6}$	AlF_3	$.32 \times 10^{-10}$	high sanidine
$NaCO_3^{-}$	$.10 \times 10^{-6}$	AlF_4^{-}	$.17 \times 10^{-12}$	high albite
$NaSO_4^{-}$	$.30 \times 10^{-5}$	AlF_6^{-3}	$.87 \times 10^{-20}$	dickite
$CaCO_3$	$.24 \times 10^{-5}$	HF	$.40 \times 10^{-9}$	halloysite
$CaHCO_3^{+}$	$.78 \times 10^{-5}$	MgF^{+}	$.14 \times 10^{-5}$	K-montmorillonite
$CaSO_4$	$.15 \times 10^{-5}$	H^{+}	$.13 \times 10^{-7}$	Ca-montmorillonite
$MgCO_3$	$.11 \times 10^{-5}$	OH^{-}	$.84 \times 10^{-6}$	Mg-montmorillonite
$MgHCO_3^{+}$	$.97 \times 10^{-6}$			spinel
$MgSO_4$	$.51 \times 10^{-5}$			andalusite
$FeCl^{+}$	$.14 \times 10^{-8}$			sillimanite
$FeSO_4$	$.39 \times 10^{-7}$			25 SW montmorillonite
				chlorite (Mg)
				laumontite
				prehnite
				wairakite
				zoisite

TABLE 15

Concentrations of Aqueous Species, Water from Below the Umtanum (Wolery code)

Species	Concentration (moles/kg)	Species	Concentration (moles/kg)	Species	Concentration (moles/kg)
Na^{+}	$.87 \times 10^{-3}$	$CaCO_3$	$.11 \times 10^{-6}$	$H_3SiO_4^{-}$	$.21 \times 10^{-5}$
K^{+}	$.23 \times 10^{-3}$	$CaHCO_3^{+}$	$.14 \times 10^{-5}$	$AlSO_4^{+}$	$.27 \times 10^{-11}$
Ca^{+2}	$.16 \times 10^{-3}$	$CaSO_4$	$.50 \times 10^{-5}$	$CuOH^{+}$	$.24 \times 10^{-6}$
Mg^{+2}	$.40 \times 10^{-4}$	$MgCO_3$	$.17 \times 10^{-7}$	HSO_4^{-}	$.10 \times 10^{-8}$
Al^{+3}	$.20 \times 10^{-10}$	$MgHCO_3^{+}$	$.25 \times 10^{-6}$	HCO_3^{-}	$.63 \times 10^{-3}$
$SiO_2(aq)$	$.37 \times 10^{-3}$	$MgSO_4$	$.11 \times 10^{-5}$	H_2CO_3	$.65 \times 10^{-4}$
Zn^{+2}	$.38 \times 10^{-4}$	$FeSO_4$	$.46 \times 10^{-15}$	HCl	$.16 \times 10^{-16}$
H^{+}	$.53 \times 10^{-7}$	$FeCl^{+2}$	$.36 \times 10^{-15}$	$MgOH^{+}$	$.11 \times 10^{-8}$
CO_3^{-2}	$.67 \times 10^{-6}$	$FeCl_2^{+}$	$.25 \times 10^{-19}$	$FeOH^{+}$	$.14 \times 10^{-14}$
Cl^{-}	$.46 \times 10^{-3}$	$FeCl_3$	$.31 \times 10^{-22}$	$CaOH^{+}$	$.67 \times 10^{-9}$
SO_4^{-2}	$.23 \times 10^{-3}$	$FeCl_4^{-}$	$.18 \times 10^{-27}$	$FeOH^{+2}$	$.43 \times 10^{-8}$
Fe^{+2}	$.17 \times 10^{-13}$	$FeSO_4^{+}$	$.46 \times 10^{-13}$	$Fe(OH)_2^{+}$	$.78 \times 10^{-6}$
Cu^{+}	$.15 \times 10^{-17}$	$ZnCl^{+}$	$.39 \times 10^{-7}$	$Fe(OH)_3^{-}$	$.12 \times 10^{-23}$
Fe^{+3}	$.43 \times 10^{-13}$	$ZnCl_2$	$.25 \times 10^{-10}$	$Fe(OH)_4^{-}$	$.56 \times 10^{-6}$
Cu^{+2}	$.71 \times 10^{-7}$	$ZnCl_3^{-}$	$.93 \times 10^{-14}$	$NaOH$	$.33 \times 10^{-10}$
OH^{-}	$.21 \times 10^{-6}$	$ZnCl_4^{-2}$	$.22 \times 10^{-17}$	$(FeOH^{+2})_2$	$.94 \times 10^{-15}$
$AlOH^{+2}$	$.58 \times 10^{-8}$	$ZnSO_4$	$.14 \times 10^{-5}$		
$Al(OH)_4^{-}$	$.14 \times 10^{-4}$	$CuCl_2^{-}$	$.25 \times 10^{-19}$		
KSO_4^{-}	$.31 \times 10^{-6}$	$CuCl_3^{-2}$	$.20 \times 10^{-22}$		
$NaCO_3^{-}$	$.44 \times 10^{-8}$	$CuCl^{+}$	$.28 \times 10^{-10}$		
$NaSO_4^{-}$	$.87 \times 10^{-6}$	$CuCl_2$	$.23 \times 10^{-14}$		
		$CuCl_3^{-}$	$.26 \times 10^{-19}$		
		$CuCl_4^{-2}$	$.66 \times 10^{-25}$		
		$CuSO_4$	$.60 \times 10^{-13}$		

TABLE 16

Concentrations of Aqueous Species, Water from Above the Umtanum (Wolery code)

Species	Concentration (moles/kg)	Species	Concentration (moles/kg)	Species	Concentration (moles/kg)
Na^{+}	$.11 \times 10^{-2}$	$CaCO_3$	$.27 \times 10^{-6}$	$H_3SiO_4^{-}$	$.27 \times 10^{-5}$
K^{+}	$.20 \times 10^{-3}$	$CaHCO_3^{+}$	$.27 \times 10^{-5}$	$AlSO_4^{+}$	$.16 \times 10^{-12}$
Ca^{+2}	$.21 \times 10^{-3}$	$CaSO_4$	$.34 \times 10^{-5}$	$CuOH^{+}$	$.63 \times 10^{-6}$
Mg^{+2}	$.88 \times 10^{-4}$	$MgCO_3$	$.71 \times 10^{-7}$	HSO_4^{-}	$.46 \times 10^{-9}$
Al^{+3}	$.24 \times 10^{-11}$	$MgHCO_3^{+}$	$.82 \times 10^{-6}$	HCO_3^{-}	$.10 \times 10^{-2}$
$SiO_2(aq)$	$.37 \times 10^{-3}$	$MgSO_4$	$.13 \times 10^{-5}$	H_2CO_3	$.81 \times 10^{-4}$
Zn^{+2}	$.58 \times 10^{-3}$	$FeSO_4$	$.43 \times 10^{-16}$	HCl	$.48 \times 10^{-16}$
H^{+}	$.42 \times 10^{-7}$	$FeCl^{+2}$	$.19 \times 10^{-15}$	$MgOH^{+}$	$.30 \times 10^{-8}$
CO_3^{-2}	$.14 \times 10^{-5}$	$FeCl_2^{+}$	$.47 \times 10^{-19}$	$FeOH^{+}$	$.31 \times 10^{-15}$
Cl^{-}	$.17 \times 10^{-2}$	$FeCl_3$	$.22 \times 10^{-21}$	$CaOH^{+}$	$.11 \times 10^{-8}$
SO_4^{-2}	$.14 \times 10^{-3}$	$FeCl_4^{-}$	$.47 \times 10^{-26}$	$FeOH^{+2}$	$.77 \times 10^{-9}$
Fe^{+2}	$.30 \times 10^{-14}$	$FeSO_4^{+}$	$.35 \times 10^{-14}$	$Fe(OH)_2^{+}$	$.17 \times 10^{-6}$
Cu^{+}	$.39 \times 10^{-17}$	$ZnCl^{+}$	$.22 \times 10^{-5}$	$Fe(OH)_3^{-}$	$.39 \times 10^{-24}$
Fe^{+3}	$.66 \times 10^{-14}$	$ZnCl_2$	$.50 \times 10^{-8}$	$Fe(OH)_4^{-}$	$.19 \times 10^{-6}$
Cu^{+2}	$.15 \times 10^{-6}$	$ZnCl_3^{-}$	$.71 \times 10^{-11}$	$NaOH$	$.50 \times 10^{-10}$
OH^{-}	$.27 \times 10^{-6}$	$ZnCl_4^{-2}$	$.65 \times 10^{-14}$	$(FeOH^{+2})_2$	$.35 \times 10^{-16}$
$AlOH^{+2}$	$.82 \times 10^{-9}$	$ZnSO_4$	$.11 \times 10^{-4}$		
$Al(OH)_4^{-}$	$.37 \times 10^{-5}$	$CuCl_2^{-}$	$.91 \times 10^{-18}$		
KSO_4^{-}	$.15 \times 10^{-6}$	$CuCl_3^{-2}$	$.29 \times 10^{-20}$		
$NaCO_3^{-}$	$.11 \times 10^{-7}$	$CuCl^{+}$	$.21 \times 10^{-9}$		
$NaSO_4^{-}$	$.60 \times 10^{-6}$	$CuCl_2$	$.64 \times 10^{-13}$		
		$CuCl_3^{-}$	$.27 \times 10^{-17}$		
		$CuCl_4^{-2}$	$.28 \times 10^{-22}$		
		$CuSO_4$	$.68 \times 10^{-13}$		

TABLE 17

Concentrations of Aqueous Species, Water from the Vantage (Wolery code)

Species	Concentration (moles/kg)	Species	Concentration (moles/kg)	Species	Concentration (moles/kg)
Na^{+}	$.60 \times 10^{-3}$	$CaCO_3$	$.11 \times 10^{-5}$	$H_3SiO_4^{-}$	$.34 \times 10^{-5}$
K^{+}	$.51 \times 10^{-3}$	$CaHCO_3^{+}$	$.86 \times 10^{-5}$	$AlSO_4^{+}$	$.36 \times 10^{-12}$
Ca^{+2}	$.68 \times 10^{-3}$	$CaSO_4$	$.62 \times 10^{-4}$	$CuOH^{+}$	$.13 \times 10^{-6}$
Mg^{+2}	$.17 \times 10^{-3}$	$MgCO_3$	$.16 \times 10^{-6}$	HSO_4^{-}	$.20 \times 10^{-8}$
Al^{+3}	$.99 \times 10^{-12}$	$MgHCO_3^{+}$	$.15 \times 10^{-5}$	HCO_3^{-}	$.97 \times 10^{-3}$
$SiO_2(aq)$	$.37 \times 10^{-3}$	$MgSO_4$	$.13 \times 10^{-4}$	H_2CO_3	$.62 \times 10^{-4}$
Zn^{+2}	$.33 \times 10^{-6}$	$FeSO_4$	$.43 \times 10^{-15}$	HCl	$.58 \times 10^{-17}$
H^{+}	$.34 \times 10^{-7}$	$FeCl^{+2}$	$.43 \times 10^{-16}$	$MgOH^{+}$	$.71 \times 10^{-8}$
CO_3^{-2}	$.17 \times 10^{-5}$	$FeCl_2^{+}$	$.16 \times 10^{-20}$	$FeOH^{+}$	$.71 \times 10^{-15}$
Cl^{-}	$.27 \times 10^{-3}$	$FeCl_3$	$.11 \times 10^{-23}$	$CaOH^{+}$	$.43 \times 10^{-8}$
SO_4^{-2}	$.78 \times 10^{-3}$	$FeCl_4^{-}$	$.37 \times 10^{-29}$	$FeOH^{+2}$	$.14 \times 10^{-8}$
Fe^{+2}	$.55 \times 10^{-14}$	$FeSO_4^{+}$	$.28 \times 10^{-13}$	$Fe(OH)_2^{+}$	$.38 \times 10^{-6}$
Cu^{+}	$.80 \times 10^{-18}$	$ZnCl^{+}$	$.19 \times 10^{-9}$	$Fe(OH)_3^{-}$	$.14 \times 10^{-23}$
Fe^{+3}	$.97 \times 10^{-14}$	$ZnCl_2$	$.66 \times 10^{-13}$	$Fe(OH)_4^{-}$	$.69 \times 10^{-6}$
Cu^{+2}	$.26 \times 10^{-7}$	$ZnCl_3^{-}$	$.14 \times 10^{-16}$	$NaOH$	$.35 \times 10^{-10}$
OH^{-}	$.34 \times 10^{-6}$	$ZnCl_4^{-2}$	$.21 \times 10^{-20}$	$(FeOH^{+2})_2$	$.12 \times 10^{-15}$
$AlOH^{+2}$	$.41 \times 10^{-9}$	$ZnSO_4$	$.34 \times 10^{-7}$		
$Al(OH)_4^{-}$	$.37 \times 10^{-5}$	$CuCl_2^{-}$	$.45 \times 10^{-20}$		
KSO_4^{-}	$.21 \times 10^{-5}$	$CuCl_3^{-2}$	$.22 \times 10^{-23}$		
$NaCO_3^{-}$	$.71 \times 10^{-8}$	$CuCl^{+}$	$.54 \times 10^{-11}$		
$NaSO_4^{-}$	$.18 \times 10^{-5}$	$CuCl_2$	$.25 \times 10^{-15}$		
		$CuCl_3^{-2}$	$.16 \times 10^{-20}$		
		$CuCl_4^{-2}$	$.26 \times 10^{-26}$		
		$CuSO_4$	$.62 \times 10^{-13}$		

TABLE 18

Concentrations of Aqueous Species, Water from Just Below the Vantage (Wolery code)

Species	Concentration (moles/kg)	Species	Concentration (moles/kg)	Species	Concentration (moles/kg)
Na^{+}	$.10 \times 10^{-2}$	$CaCO_3$	$.23 \times 10^{-5}$	$H_3SiO_4^{-}$	$.78 \times 10^{-5}$
K^{+}	$.47 \times 10^{-3}$	$CaHCO_3^{+}$	$.72 \times 10^{-5}$	$AlSO_4^{+}$	$.39 \times 10^{-14}$
Ca^{+2}	$.36 \times 10^{-3}$	$CaSO_4$	$.15 \times 10^{-4}$	$CuOH^{+}$	$.23 \times 10^{-6}$
Mg^{+2}	$.11 \times 10^{-3}$	$MgCO_3$	$.40 \times 10^{-6}$	HSO_4^{-}	$.34 \times 10^{-9}$
Al^{+3}	$.23 \times 10^{-13}$	$MgHCO_3^{+}$	$.15 \times 10^{-5}$	HCO_3^{-}	$.15 \times 10^{-2}$
$SiO_2(aq)$	$.35 \times 10^{-3}$	$MgSO_4$	$.37 \times 10^{-5}$	H_2CO_3	$.38 \times 10^{-4}$
Zn^{+2}	$.77 \times 10^{-6}$	$FeSO_4$	$.26 \times 10^{-16}$	HCl	$.23 \times 10^{-17}$
H^{+}	$.13 \times 10^{-7}$	$FeCl^{+2}$	$.23 \times 10^{-17}$	$MgOH^{+}$	$.11 \times 10^{-7}$
CO_3^{-2}	$.64 \times 10^{-5}$	$FeCl_2^{+}$	$.86 \times 10^{-22}$	$FeOH^{+}$	$.25 \times 10^{-15}$
Cl^{-}	$.26 \times 10^{-3}$	$FeCl_3$	$.60 \times 10^{-25}$	$CaOH^{+}$	$.60 \times 10^{-8}$
SO_4^{-2}	$.32 \times 10^{-3}$	$FeCl_4^{-}$	$.19 \times 10^{-30}$	$FeOH^{+2}$	$.19 \times 10^{-9}$
Fe^{+2}	$.75 \times 10^{-15}$	$FeSO_4^{+}$	$.67 \times 10^{-15}$	$Fe(OH)_2^{+}$	$.13 \times 10^{-6}$
Cu^{+}	$.14 \times 10^{-17}$	$ZnCl^{+}$	$.44 \times 10^{-9}$	$Fe(OH)_3$	$.32 \times 10^{-23}$
Fe^{+3}	$.51 \times 10^{-15}$	$ZnCl_2$	$.15 \times 10^{-12}$	$Fe(OH)_4^{-}$	$.15 \times 10^{-5}$
Cu^{+2}	$.18 \times 10^{-7}$	$ZnCl_3^{-}$	$.33 \times 10^{-16}$	$NaOH$	$.15 \times 10^{-9}$
OH^{-}	$.83 \times 10^{-6}$	$ZnCl_4^{-2}$	$.45 \times 10^{-20}$	$(FeOH^{+2})_2$	$.21 \times 10^{-17}$
$AlOH^{+2}$	$.25 \times 10^{-10}$	$ZnSO_4$	$.36 \times 10^{-7}$		
$Al(OH)_4^{-}$	$.37 \times 10^{-5}$	$CuCl_2^{-}$	$.77 \times 10^{-20}$		
KSO_4^{-}	$.85 \times 10^{-6}$	$CuCl_3^{-2}$	$.36 \times 10^{-23}$		
$NaCO_3^{-}$	$.46 \times 10^{-7}$	$CuCl^{+}$	$.38 \times 10^{-11}$		
$NaSO_4^{-}$	$.13 \times 10^{-5}$	$CuCl_2$	$.17 \times 10^{-15}$		
		$CuCl_3^{-}$	$.11 \times 10^{-20}$		
		$CuCl_4^{-2}$	$.16 \times 10^{-26}$		
		$CuSO_4$	$.19 \times 10^{-13}$		

TABLE 19

Minerals Supersaturated in Groundwaters, according to Wolery Code

Mineral	Location of Groundwater[1] BU	U	V	BV
celadonite	S[2]	S	S	S
magnetite	S	S	S	S
corundum	S	S	S	
hematite	S	S	S	S
gibbsite	S	S	S	S
Reykjanes smectite	S	S	S	S
quartz	S	S	S	S
maximum microcline	S	S	S	S
low albite	S	S	S	S
14A-amesite	S	S	S	S
analcime	S	S	S	S
kaolinite	S	S	S	S
pyrophyllite	S	S	S	S
Na-beidellite	S	S	S	S
muscovite	S	S	S	S
illite	S	S	S	S
zoisite	S	S	S	S
kyanite	S	S	S	S
phlogopite				S
K-feldspar	S	S	S	S
high sanidine	S	S	S	S
high albite	S	S	S	S
M/T smectite-1	S	S	S	S
K-beidellite	S	S	S	S
Ca-beidellite	S	S	S	S
Mg-beidellite	S	S	S	S
tenorite		S		S
H-beidellite	S	S	S	S
M/T smectite-2	S	S	S	S
Na-saponite				S
K-saponite				S
clinozoisite	S	S	S	S
paragonite	S	S	S	S
diaspore	S	S	S	S
Ca-saponite				S
boehmite	S	S	S	S
chalcedony	S	S	S	S
Mg-saponite				S
alunite	S			
andalusite	S	S	S	S
H-saponite				S

(continued on next page)

TABLE 19 (cont.)

Minerals Supersaturated in Groundwaters, according to Wolery Code

Mineral	Location of Groundwater[1] BU	U	V	BV
14A-clinochlore				S[2]
smithsonite		S		
Na-nontronite	S	S	S	S
K-nontronite	S	S	S	S
albite	S	S	S	S
ordered epidote	S	S	S	S
andradite	S	S	S	S
Ca-nontronite	S	S	S	S
Mg-nontronite	S	S	S	S
H-nontronite	S	S	S	S
cristobalite	S	S	S	S
equilibrium epidote	S	S	S	S
wairakite	S	S	S	S
laumontite	S	S	S	S
margarite	S	S	S	S

NOTES

1) BU: water from below the Umtanum
U: water from above the Umtanum
V: water from the Vantage
BV: water from just below the Vantage

2) "S" signifies that the mineral was found to be supersaturated in the groundwater.

TABLE 20

Optimum Mineral Assemblages to Remove Supersaturations

In Hanford Groundwaters (Wolery code)

Source of Groundwater	Mineral Assemblage
Below Umtanum	muscovite ($KAl_3Si_3O_{10}(OH)_2$)
	chalcedony (SiO_2)
	Ca-nontronite ($Ca_{.165}Al_{.33}Si_{3.67}Fe_2O_{10}(OH)_2$)
Umtanum	kaolinite ($Al_2Si_2O_5(OH)_4$)
	chalcedony
	Ca-nontronite
	smithsonite ($ZnCO_3$)
Vantage	maximum microcline ($KAlSi_3O_8$)
	chalcedony
	Ca-nontronite
Below Vantage	celadonite ($KMgAlSi_4O_{10}(OH)_2$)
	chalcedony
	Ca-nontronite
	tenorite (CuO)

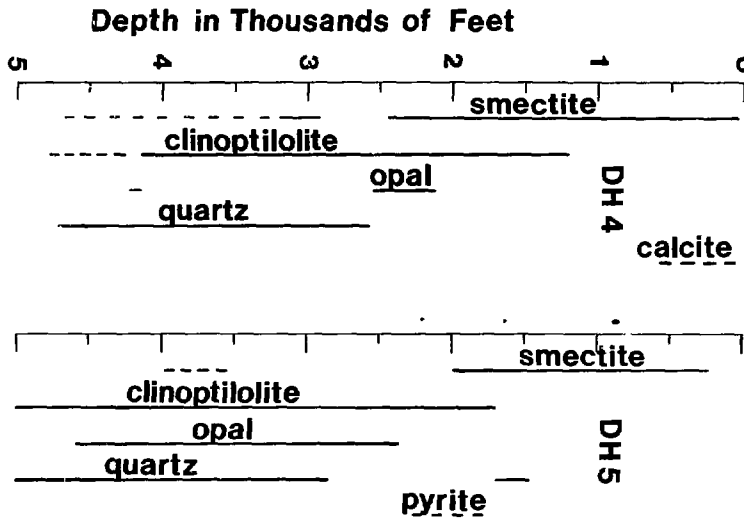

XBL 789-10901

Figure 1

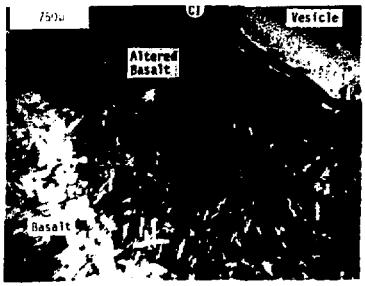

DC2 2448

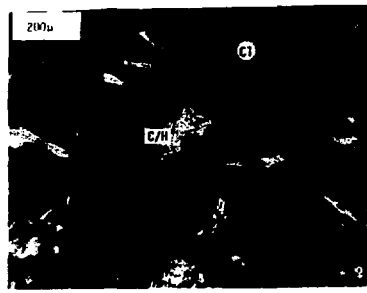

DC2 2448

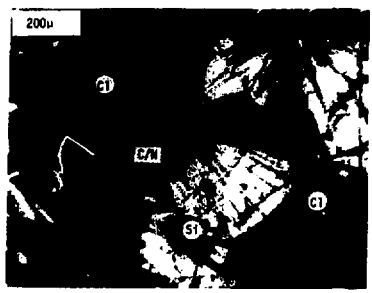

DC2 2413

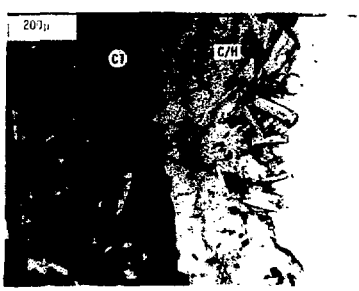

DC2 2366

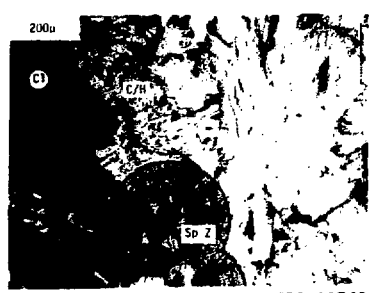

XBB 789 10763

DC2 2366

Figure 2

DC2 3264

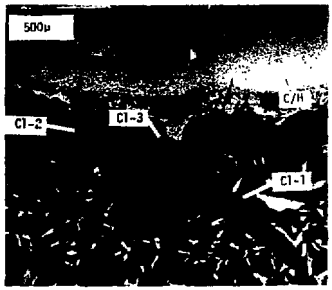

DC2 3264

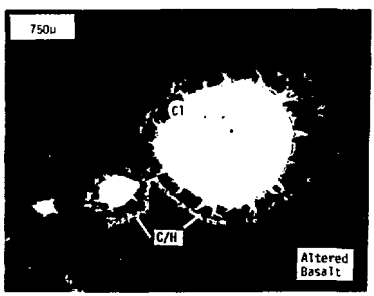

DC2 2637

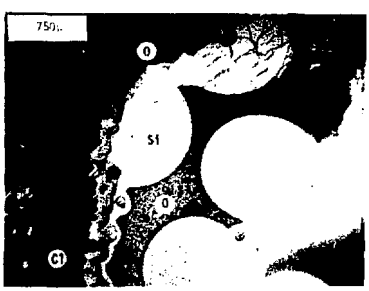

DC2 2448

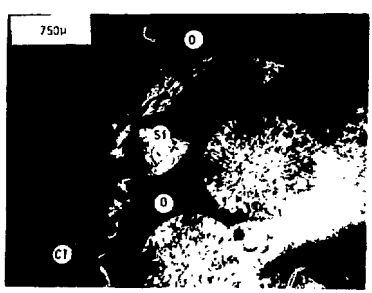

DC2 2448

Figure 3
XBB 789 10764

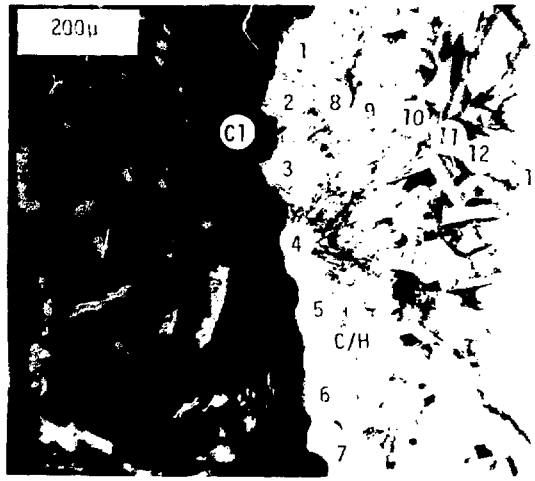

DC2 2366

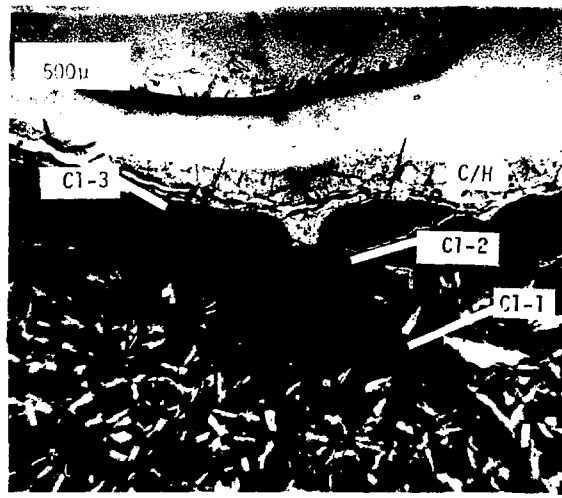

DC2 3264

Figure 4
XBB 789 10765

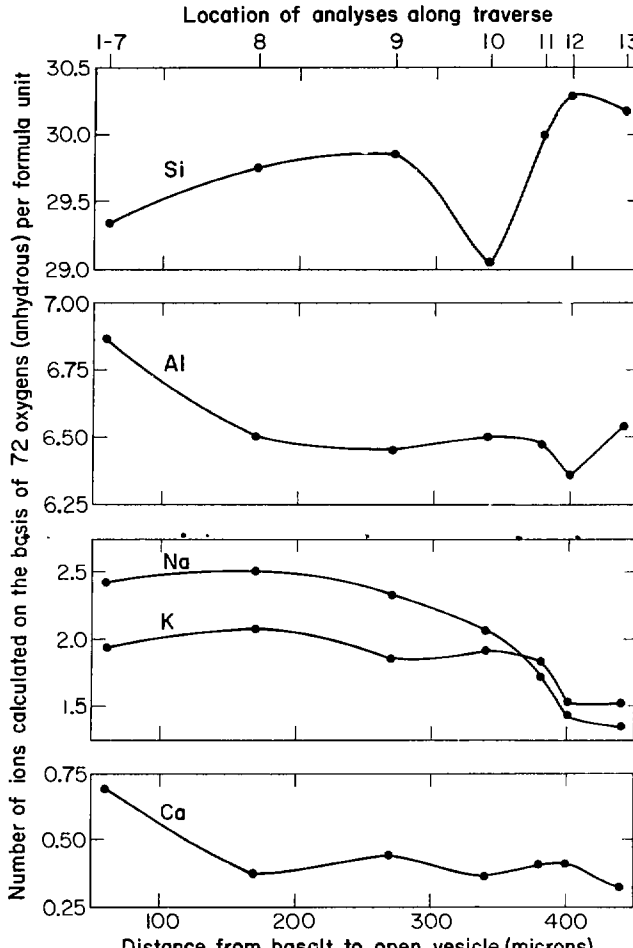

XBL 789-10902

Figure 5

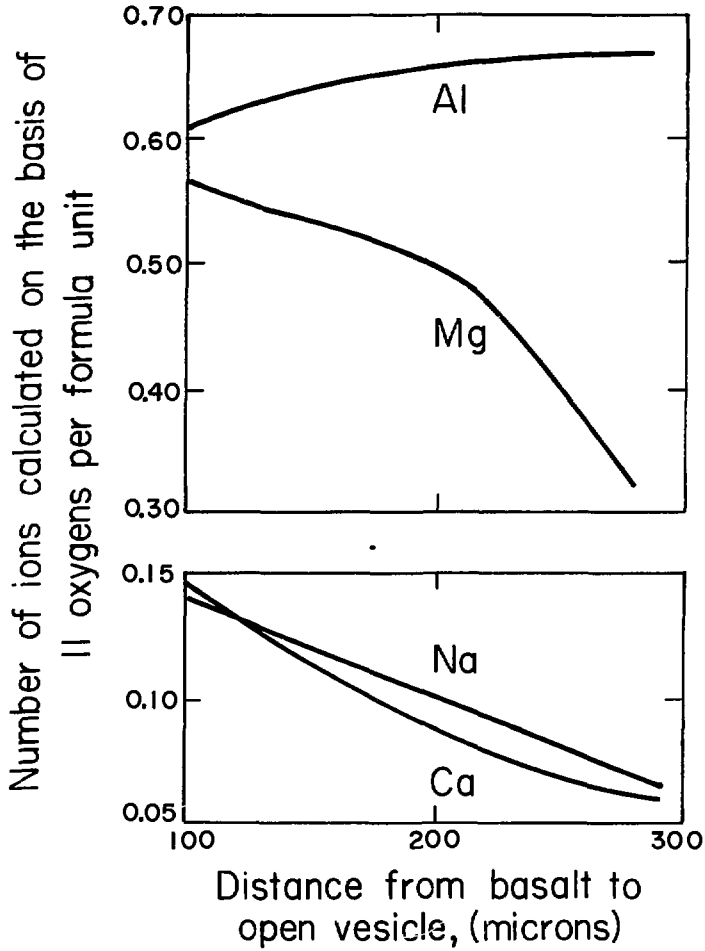

XBL 789-1797

Figure 6a

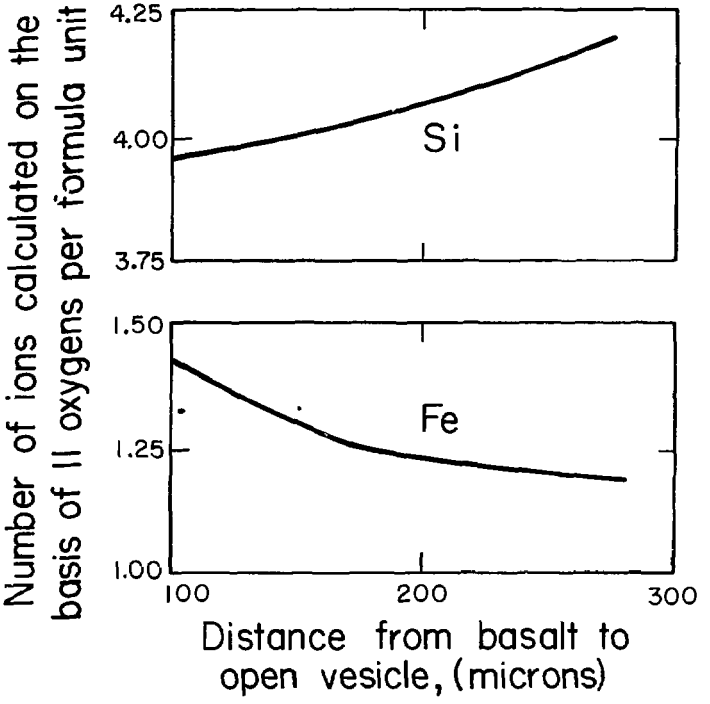

XBL 789-1798

Figure 6b

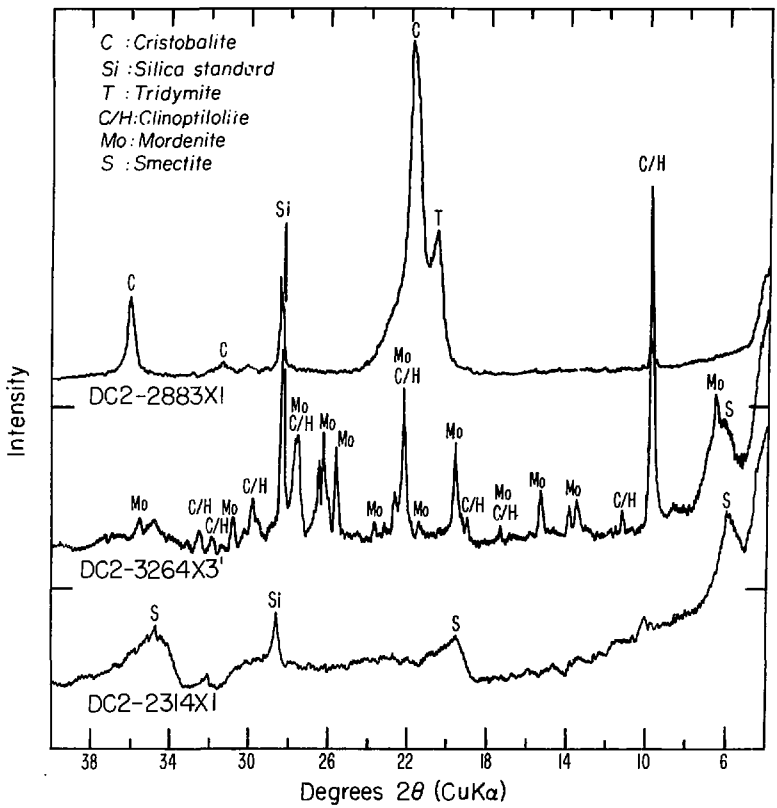

XBL 789-2676

Figure 7

DC2 2206 (S1)

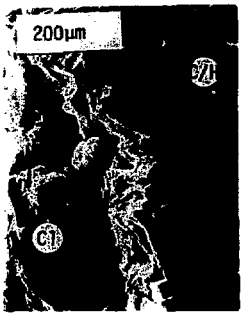

DC2 2206 (S2A)

DC2 2206 (S2B)

DC2 2206 (S3)

DC2 2206 (S3)

DC2 2359 (S2A)

DC2 2749 (S1B)

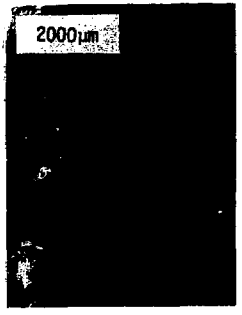

DC2 2960 (S2)

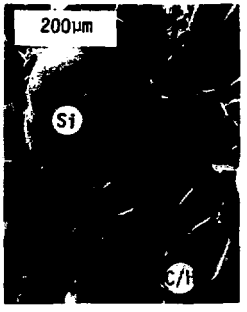

DC2 2960 (S2)

Figure 8
XBB 788 10624

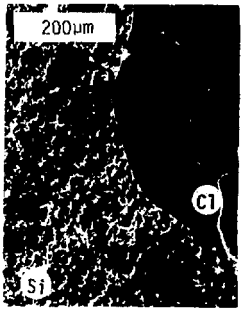

DC2 2282 (S1)

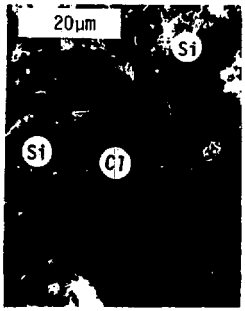

DC2 2282 (S1)

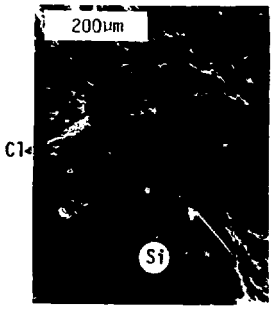

DC2 2347 (S1)

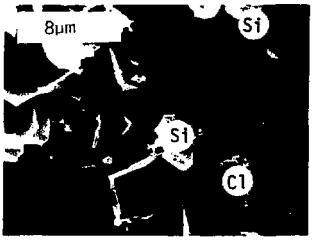

DC2 2448 (S2A)

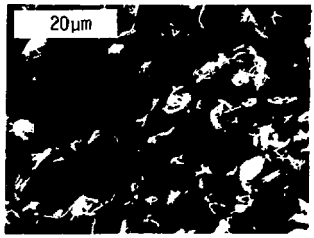

DC2 2507 (S1)

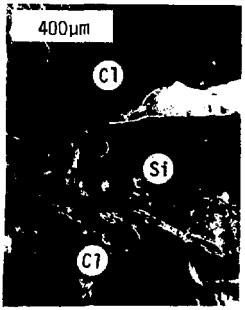

DC2 2561 (S1)

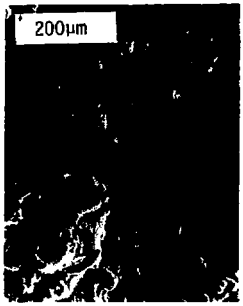

DC2 2666 (S1E)

DC2 2666 (S1E)

Figure 9

XBB 788-10628

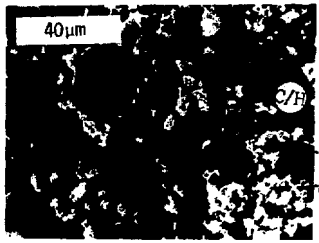

DC2 2803 (S2)

DC2 2803 (S2)

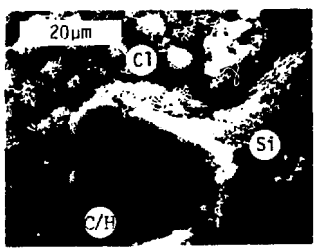

DC2 2803 (S1)

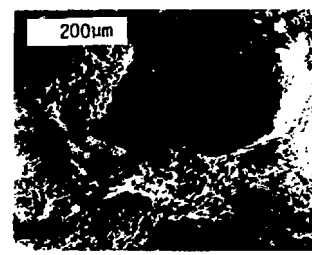

DC2 2955 (S3)

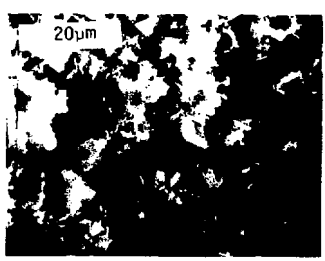

DC2 2955 (S3)

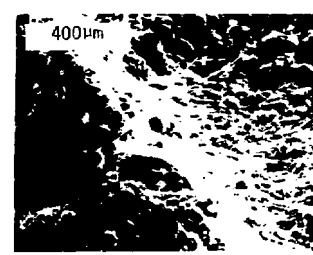

DC2 2960 (S1B)

Figure 10
XBB 788 10625

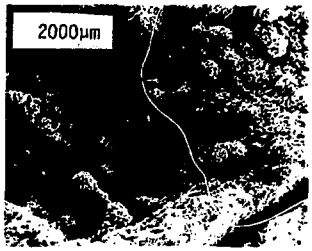

DC2 2319 (S4A)

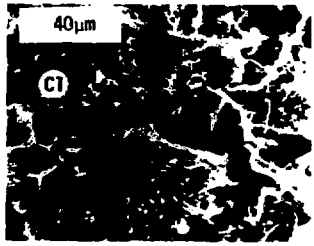

DC2 2319 (S4A)

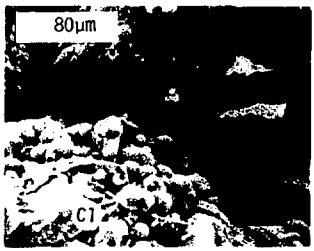

DC2 2319 (S5C)

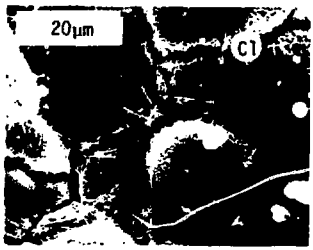

DC2 2448 (S1)

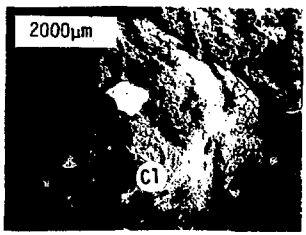

DC2 3181 (S1)

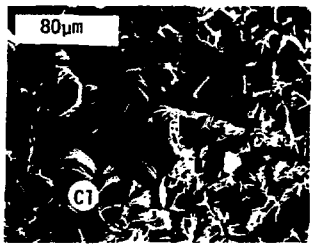

DC2 3181 (S1)

Figure 11
XBB 788 10623

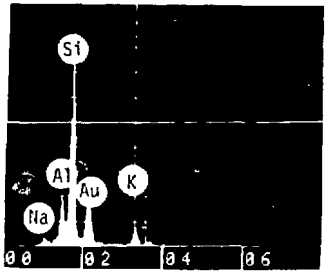

DC2 2206 (S2)

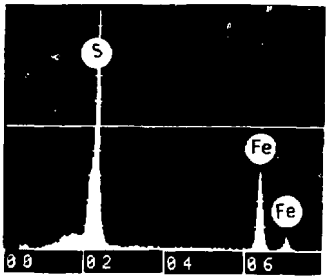

DC2 2354 (S1)

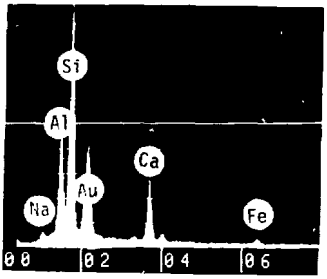

DC2 2366 (S1B)

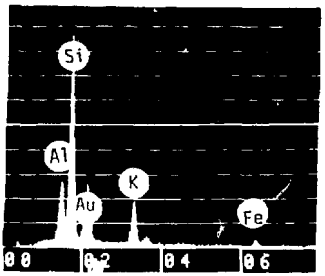

DC2 2366 (S1)

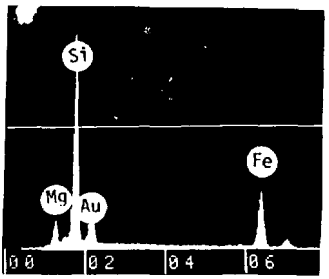

DC2 2561 (S1)

Figure 12
XBB 788 10621

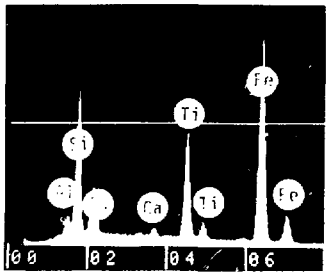

DC2 2561 (S1)

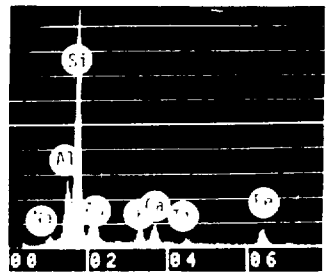

DC2 2448 (S1)

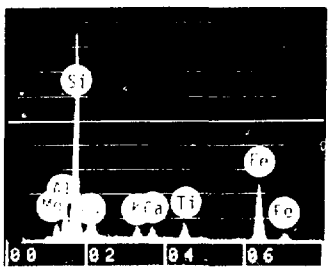

DC2 2632 (S3B)

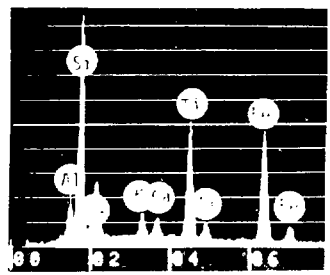

DC2 3264 (S1)

XBB 788 10620

BG2 2366 (S1A)

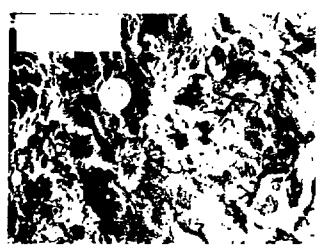

BG2 2366 (S1B)

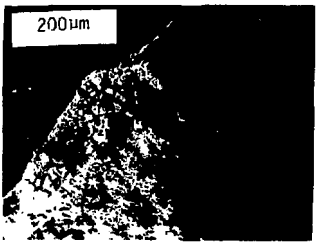

DC2 2632 (S1)

DC2 2632 (S1A)

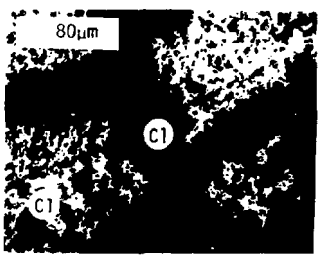

DC2 2632 (S1A)

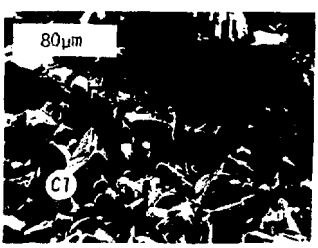

DC2 2632 (S1A)

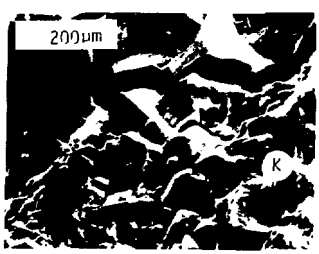

DC2 2632 (S1A)

Figure 15
XBB 788 10617

DC2 2632 (S3B)

DC2,2632 (S3B)

DC2 2632 (S3B)

DC2 2632 (S3B)

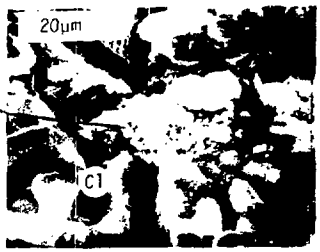

DC2 2632 (S3B)

DC2 2632 (S3C)

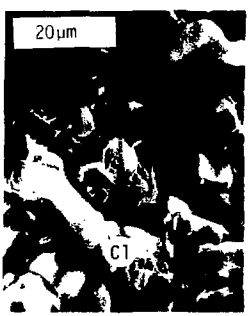

DC2 2632 (S3C)

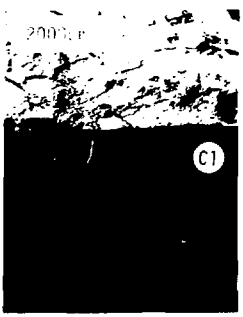

DC2 2632 (S2B)

Figure 16
X8B 788 10622

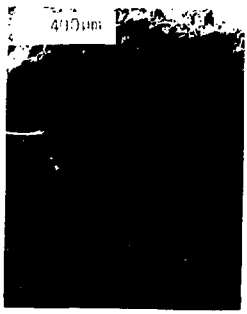

DC2 2632 (S3D)

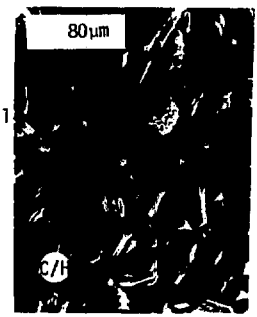

DC2 2632 (S3D)

DC2 2632 (S3D)

DC2 2632 (S3A)

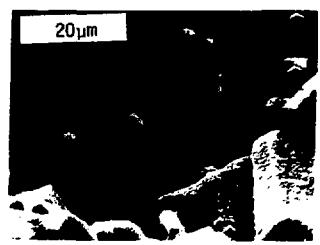

DC2 2632 (S3A)

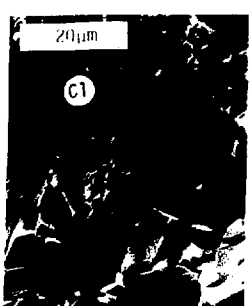

DC2 2632 (S3D)

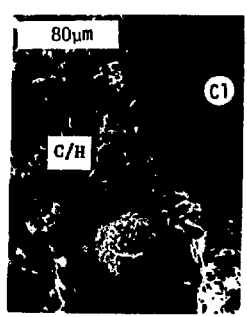

DC2 2632 (S3E)

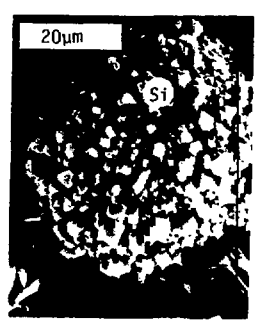

DC2 2632 (S3E)

Figure 17

XBB 788-10627

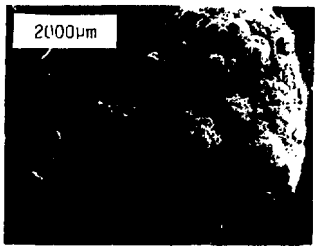

DC2 2883 (S1)

DC2 2883 (S1)

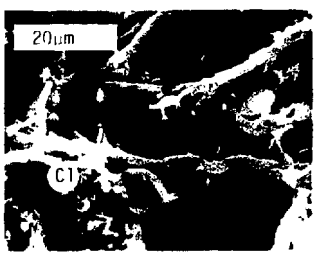

DC2 2883 (S1)

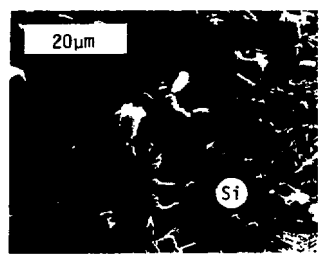

DC2 2883 (S1)

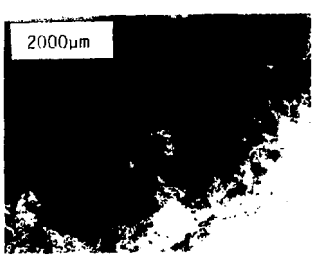

DC2 3264 (S4)

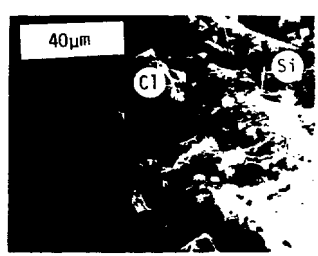

DC2 3264 (S4)

Figure 18

XBB 788 10618

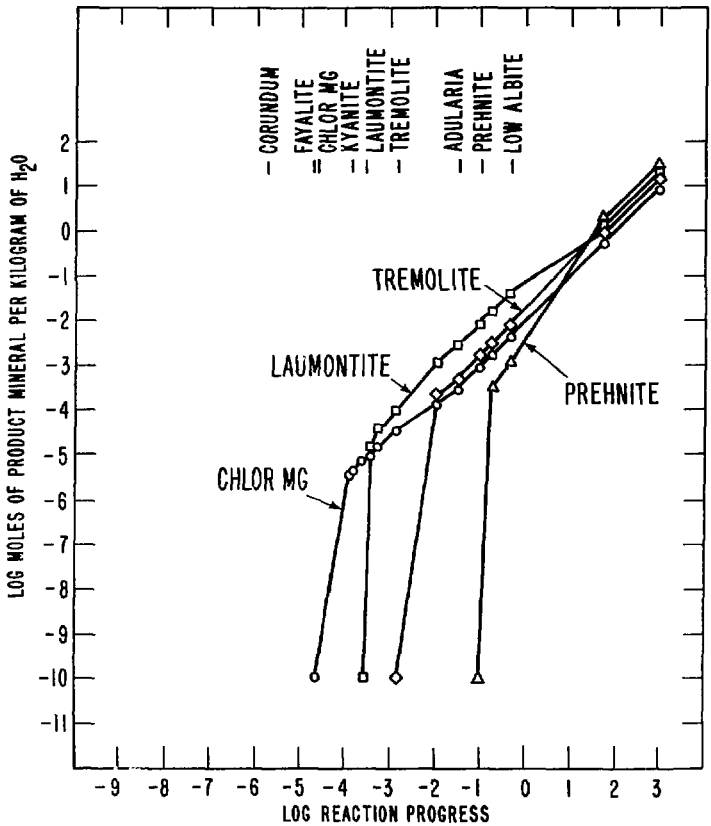

XBL789-1763

Figure 19

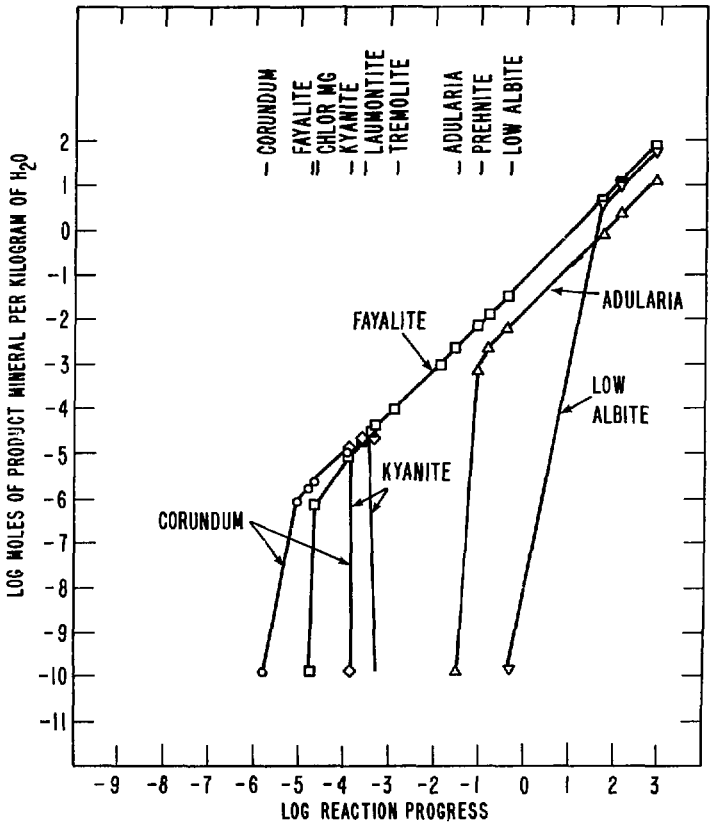

XBL 789—1748

Figure 20

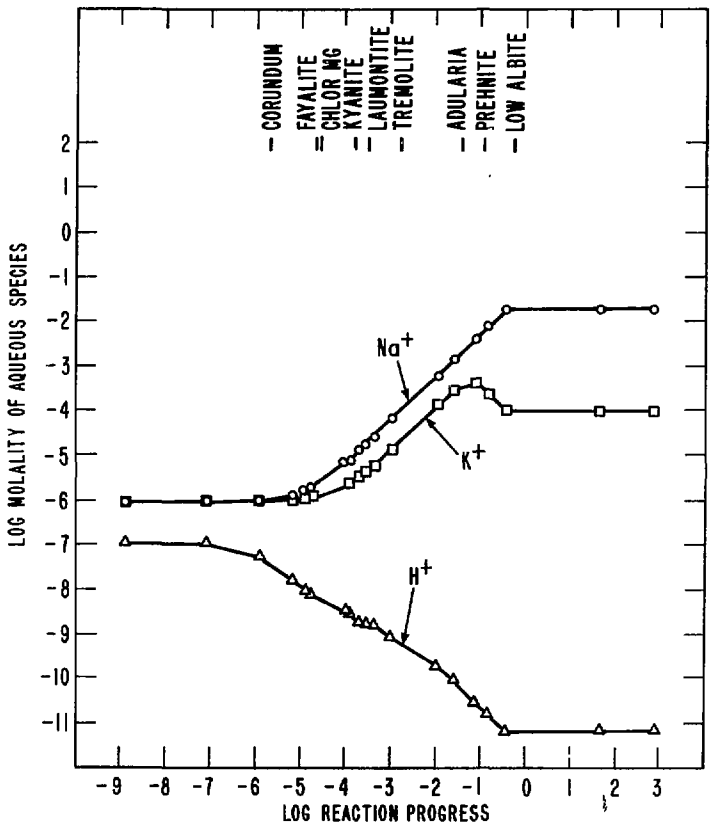

XBL 789 - 1746

Figure 21

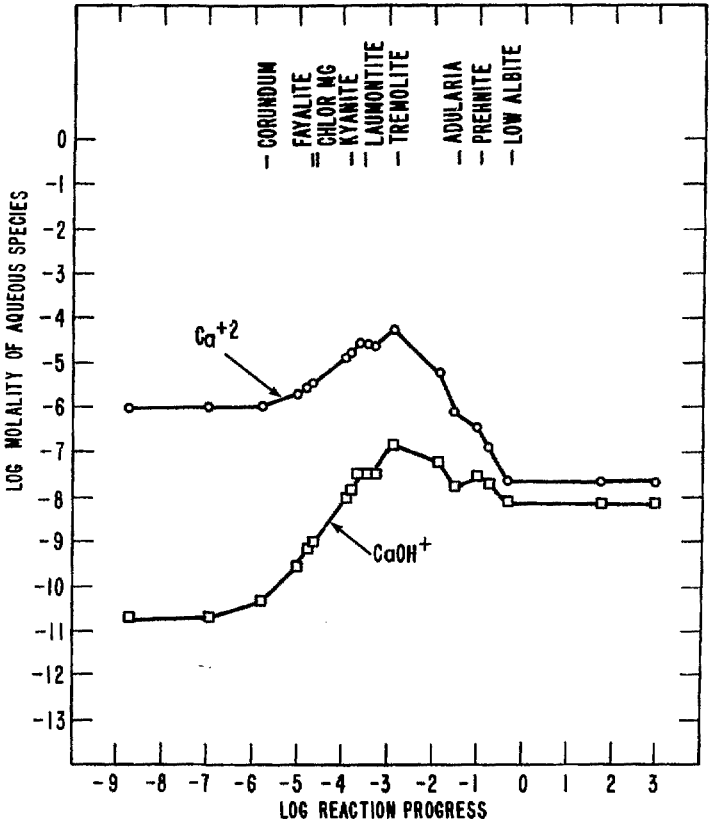

XBL 789-1751

Figure 22

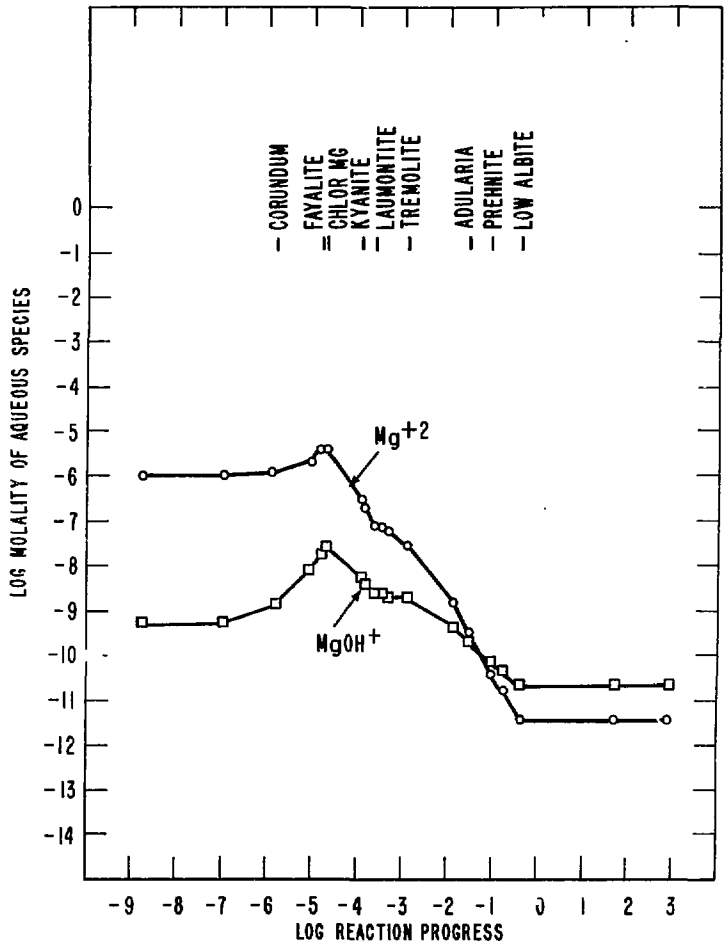

XBL789-1752

Figure 23

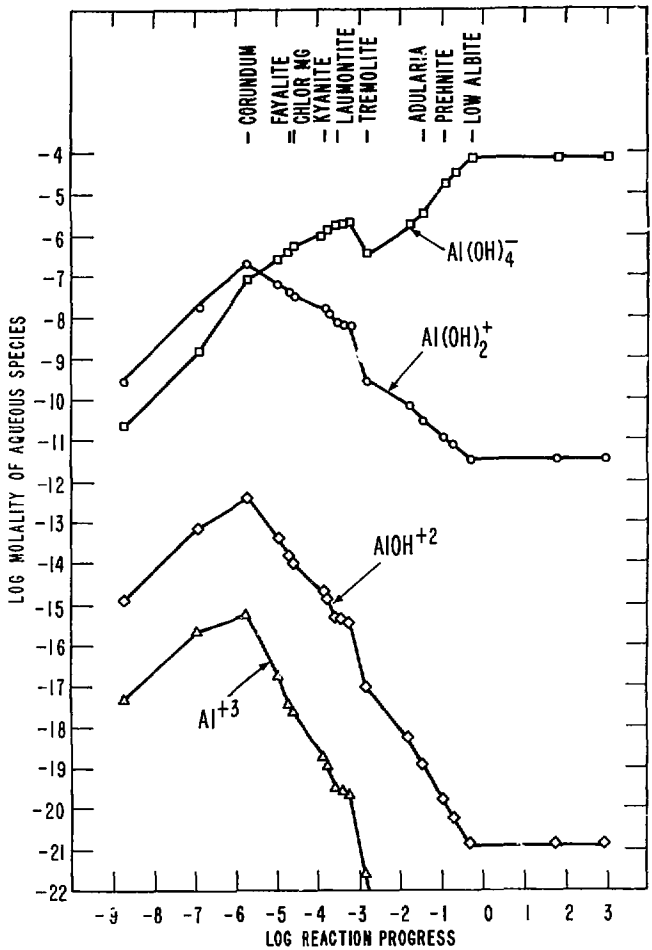

XBL 789-1759

Figure 24

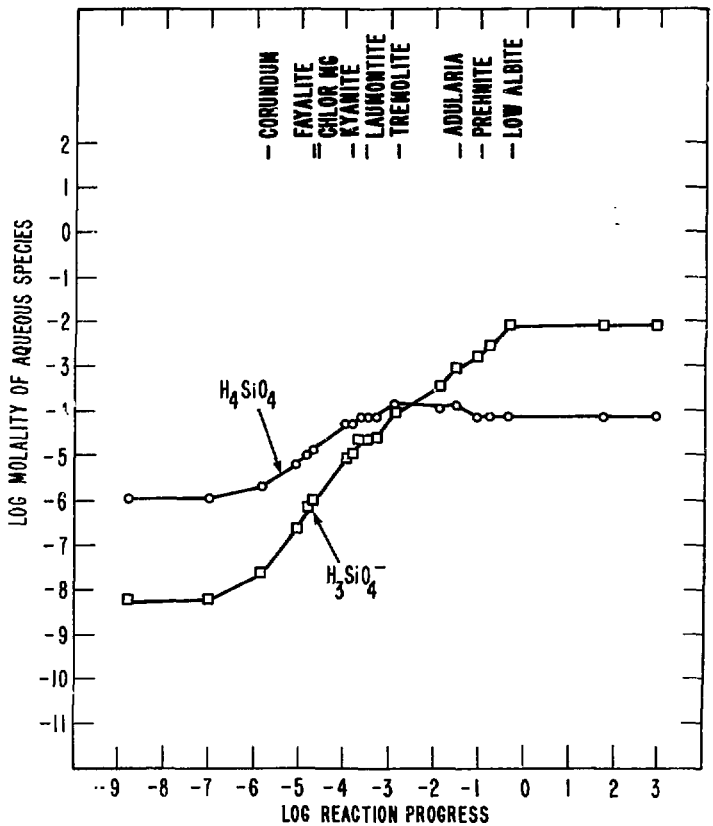

XBL 789-1749

Figure 25

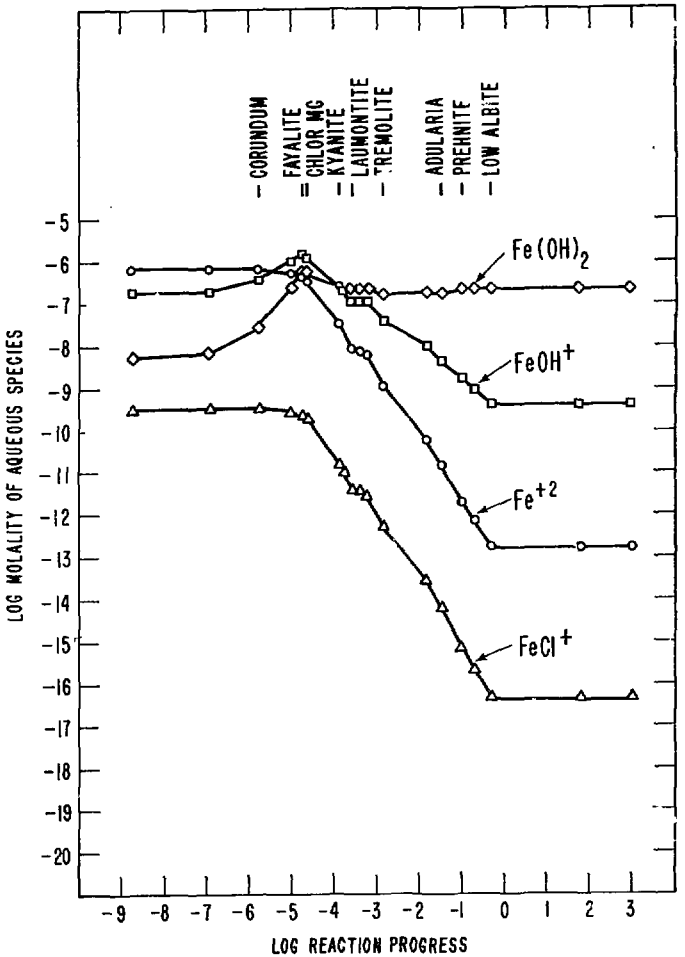

XBL 789-1762

Figure 26

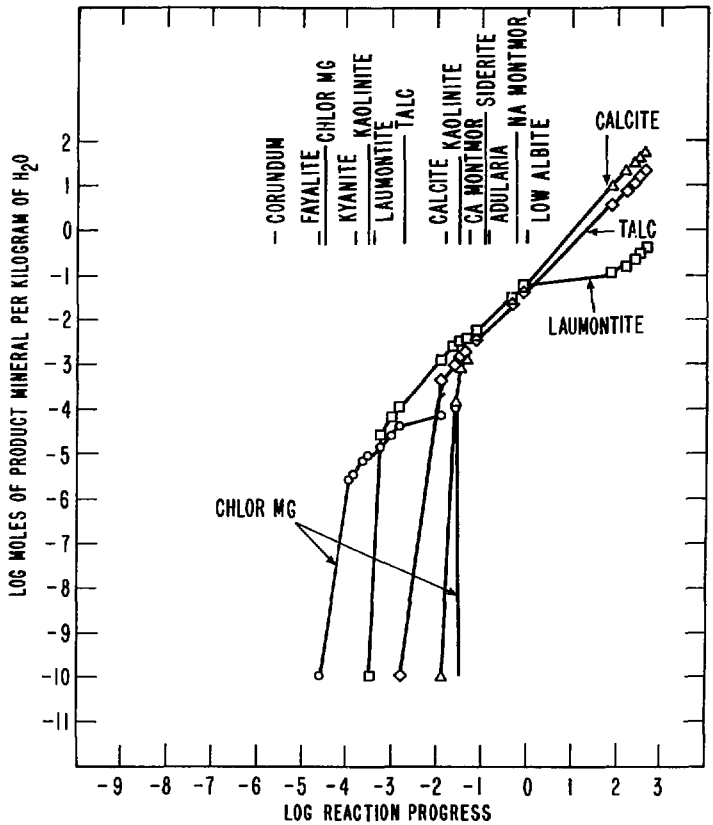

XBL789-1750

Figure 27

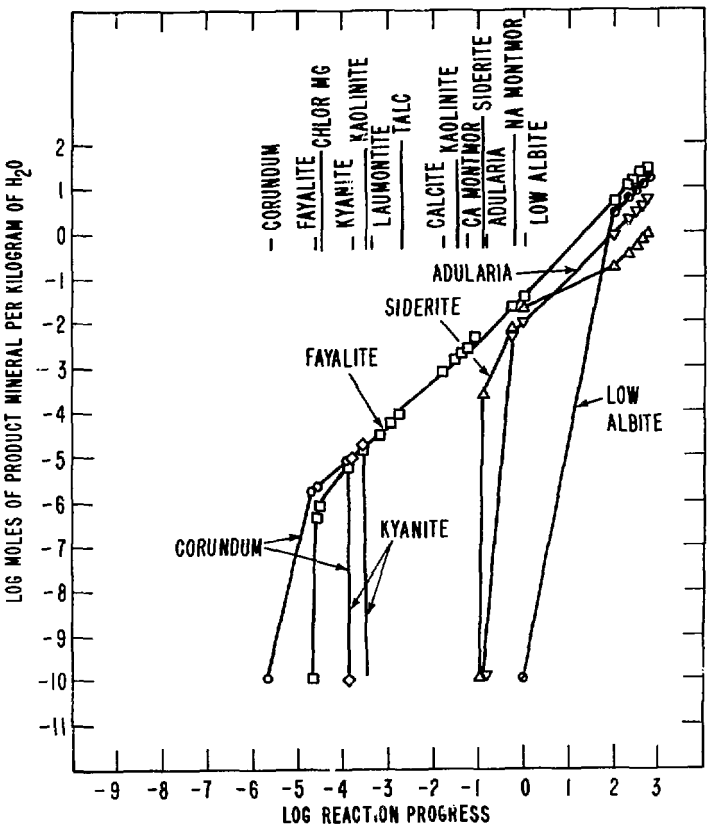

XBL 789-1747

Figure 28

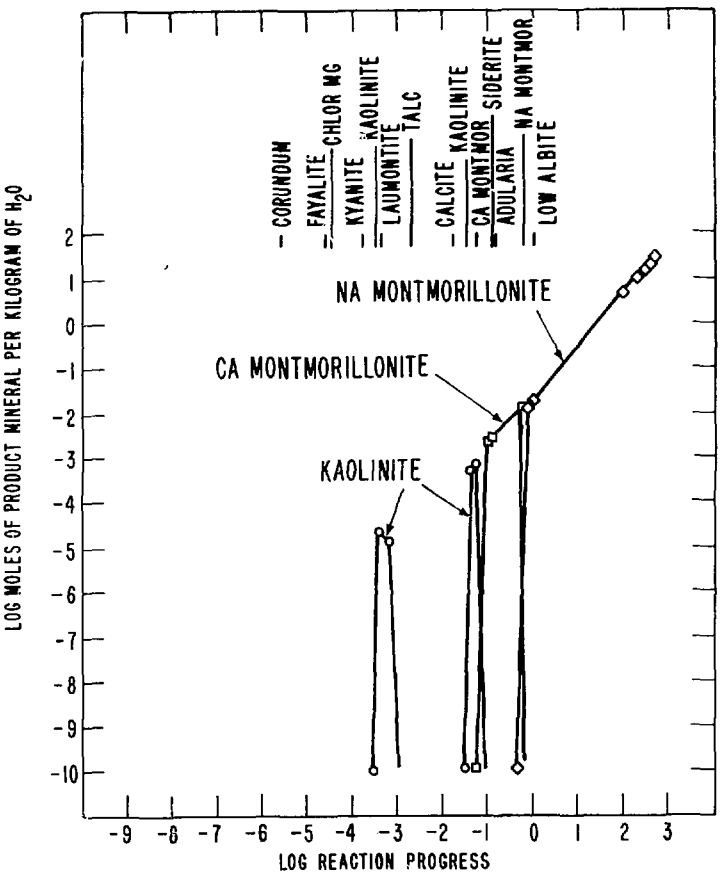

XBL789 - 1756

Figure 29

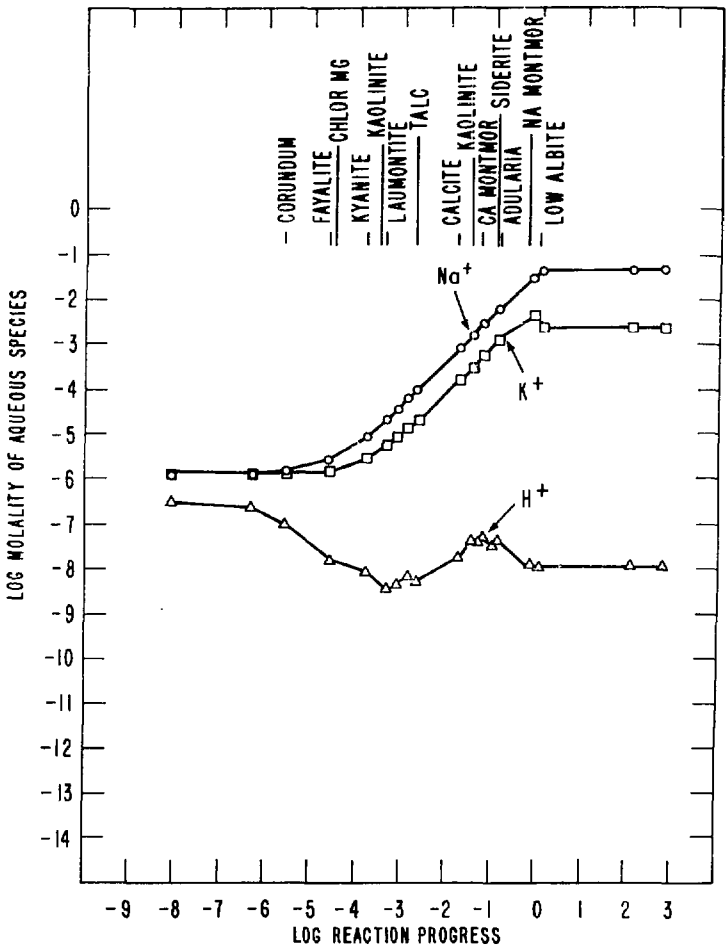

XBL 789-1754

Figure 30

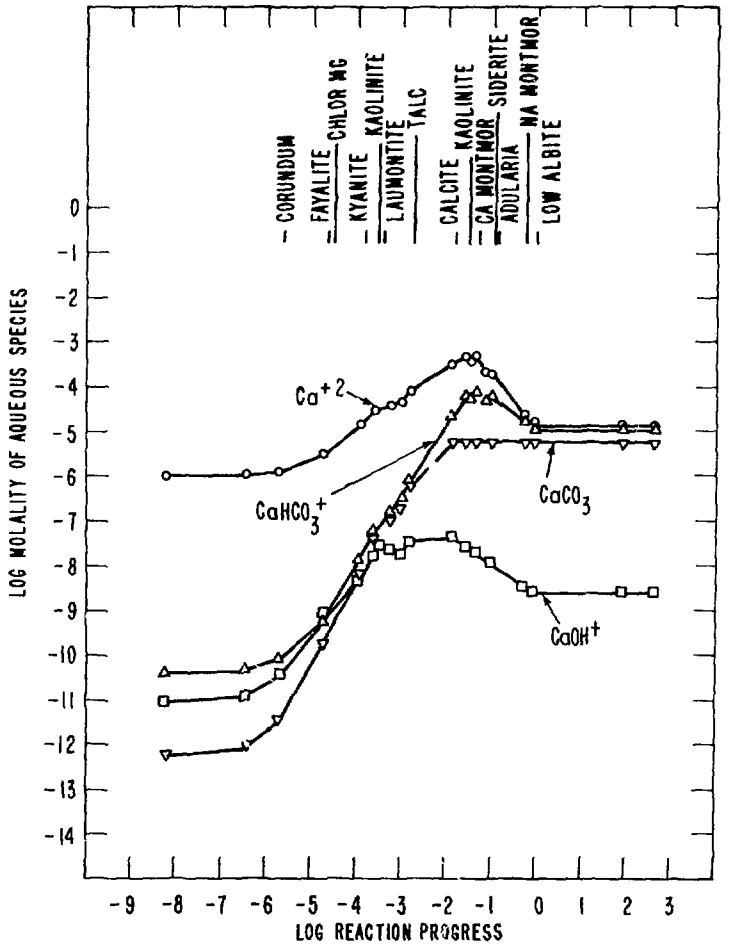

XBL789-1753

Figure 31

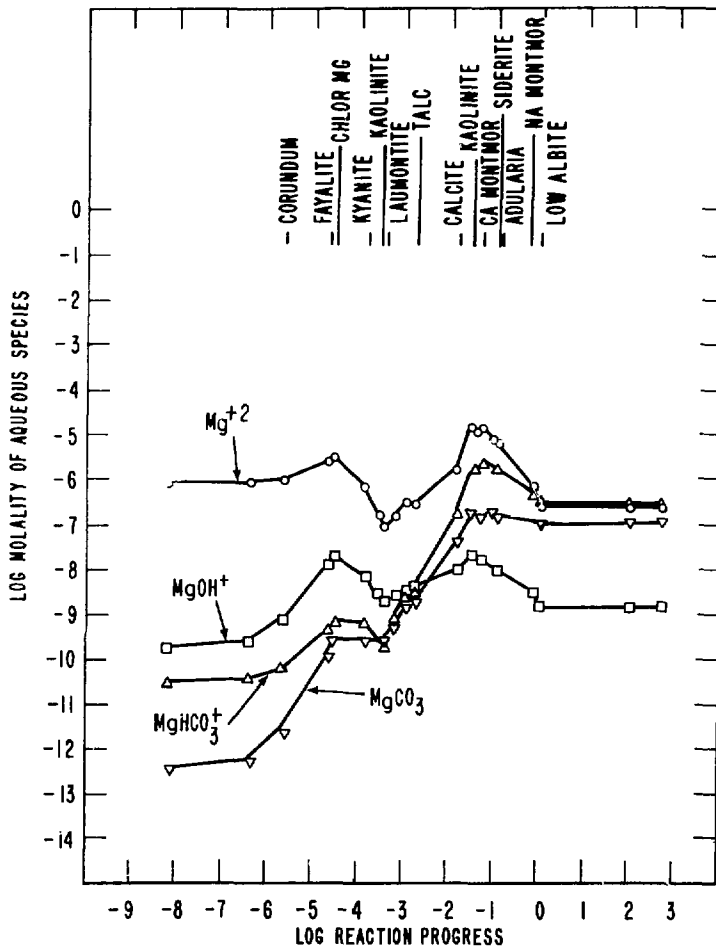

XBL789-1755

Figure 32

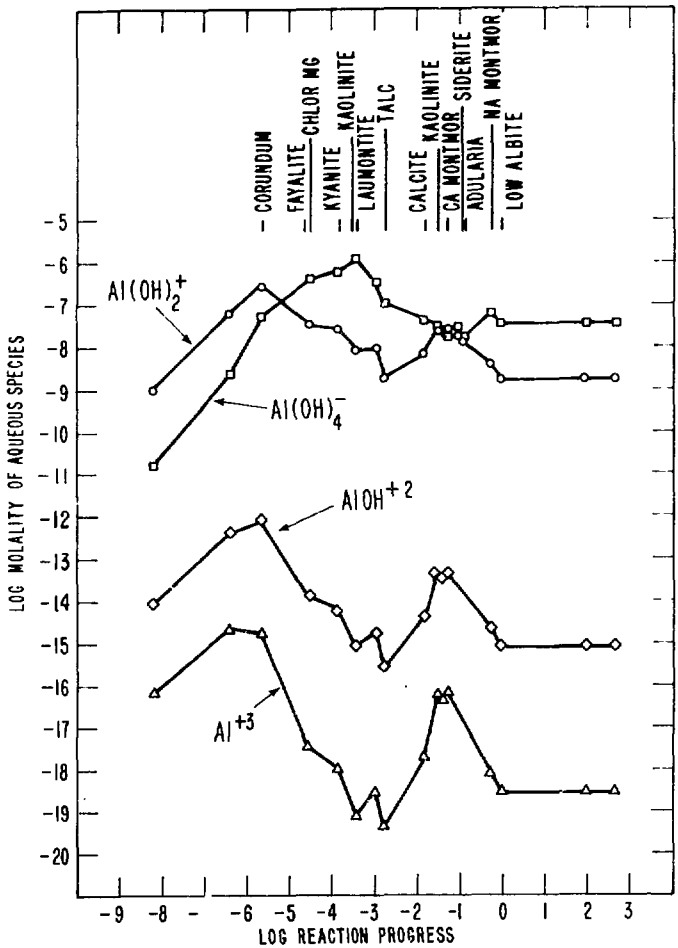

XBL789-1760

Figure 33

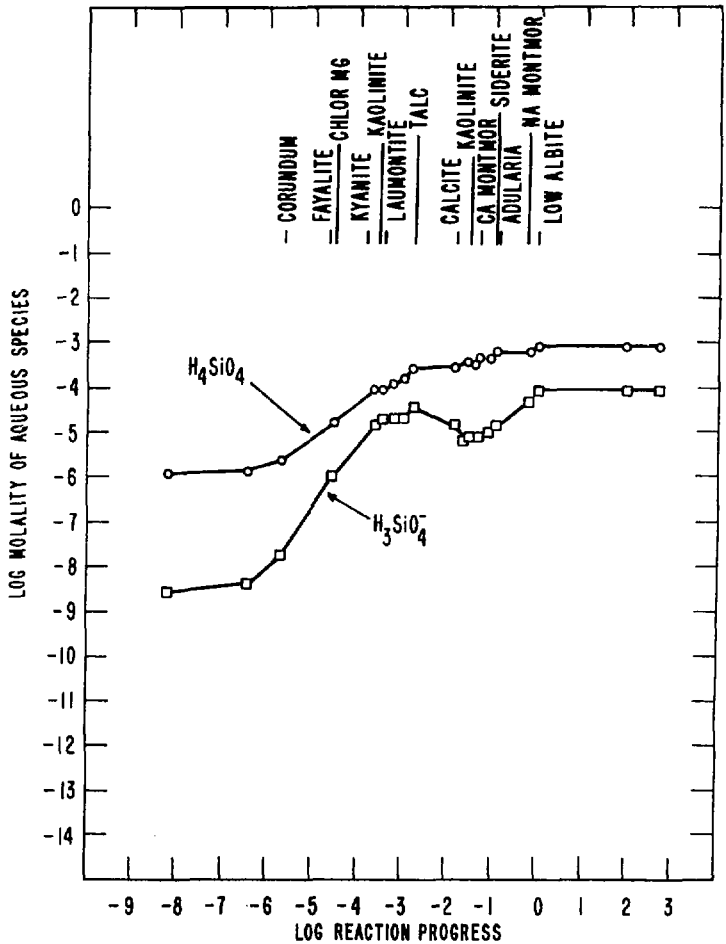

XBL789-1757

Figure 34

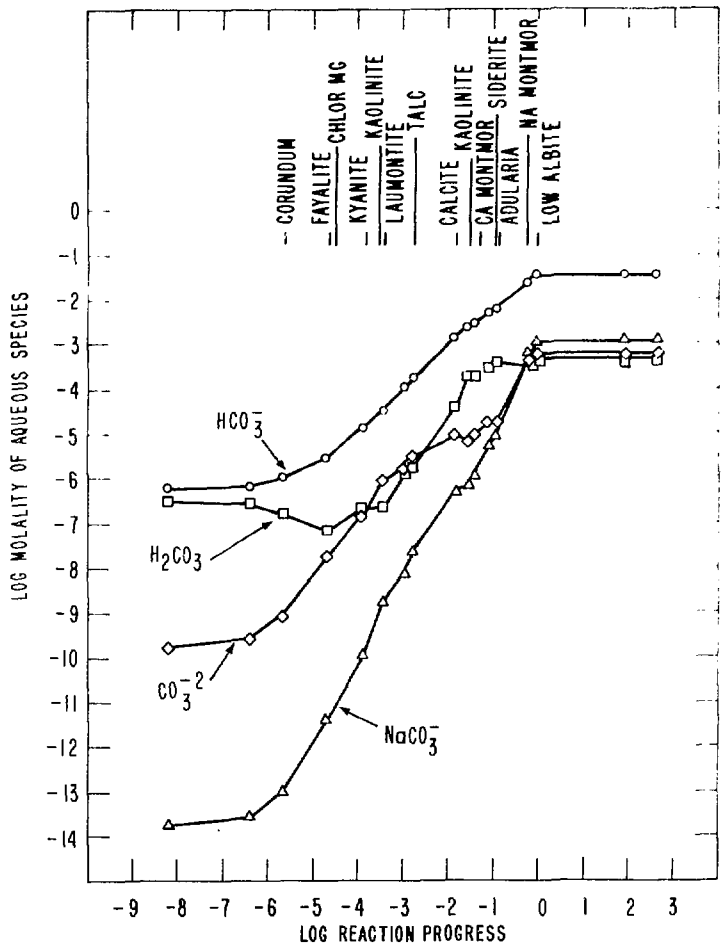

XBL789-1761

Figure 35

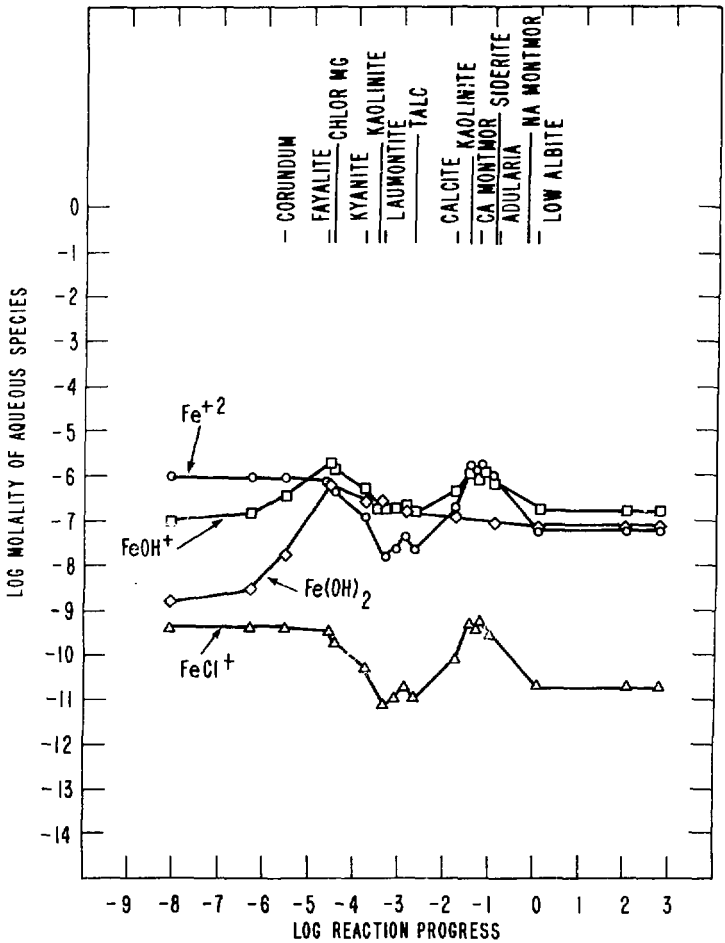

XBL789-1758

Figure 36